

ON THE APPLICATION OF PSEUDOSPECTRAL FFT TECHNIQUES TO NON-PERIODIC PROBLEMS

S. BIRINGEN AND K. H. KAO

Department of Aerospace Engineering Sciences, University of Colorado, Boulder, CO 80309, U.S.A.

SUMMARY

The reduction-to-periodicity method using the pseudospectral fast Fourier transform (FFT) technique is applied to the solution of non-periodic problems, including the two-dimensional incompressible Navier–Stokes equations. The accuracy of the method is explored by calculating the derivatives of given functions, one- and two-dimensional convective–diffusive problems, and by comparing the relative errors due to the FFT method with a second-order finite difference (FD) method. Finally, the two-dimensional Navier–Stokes equations are solved by a fractional step procedure using both the FFT and the FD methods for the driven cavity flow and the backward-facing step problems. Comparisons of these solutions provide a realistic assessment of the FFT method.

KEY WORDS Pseudospectral Non-periodic Incompressible flows

1. INTRODUCTION

In this paper we discuss a numerical technique for solving partial differential equations in non-periodic domains by the use of the pseudospectral method. This work was motivated by the need to develop a time-dependent incompressible Navier–Stokes solver with non-periodic inflow/outflow boundary conditions involving wave propagation problems. In such problems the use of Chebyshev expansions along the streamwise direction provides an accurate solution procedure at the cost of imposing very stiff viscous time step restrictions. Note that along the streamwise direction, time-explicit methods can be efficiently used owing to the absence of any sharp gradients at inflow/outflow boundaries. In flows bounded by solid walls, however, it is expected that the spectral Chebychev method will be superior for the same number of grid points and the same operation count. The goal of this paper is to provide a direct comparison of the reduction-to-periodicity method with a widely used second-order finite difference method in an effort to isolate the advantages/shortcomings of the reduction-to-periodicity method.

In periodic domains the use of the pseudospectral fast Fourier transform technique was instigated by the work of Orszag,^{1–3} and since then the method has been extensively used in solving multidimensional fluid dynamics problems with periodic boundary conditions. The article by Orszag and Israeli⁴ provides other references and an introduction to the subject. The idea of polynomial subtraction for the purpose of satisfying non-periodic boundary constraints was introduced by Lanczos⁵ and later developed by Gottlieb and Orszag.⁶ In one-dimensional model problems the well known Gibbs phenomenon that appears at the boundaries when such methods are used with non-periodic boundary conditions has been shown to be suppressed by the use of simple polynomials.^{7,8} In Reference 8 the accuracy of the reduction-to-periodicity method is

found to be the same as a Chebyshev pseudospectral method when used in one-dimensional atmospheric diffusion problems. An application of this method to the solution of the Navier–Stokes equations with non-periodic inflow/outflow boundary conditions is given in Reference 9, where the major focus was to modify the existing periodic spectral codes for use in non-periodic domains. Consequently, the implicit Crank–Nicolson method implemented for the viscous terms dictated the use of only low-order (first-order) polynomials. It should be noted that, according to Roache,⁷ the reduction-to-periodicity technique has a higher accuracy than fourth-order finite difference methods when used with high-order polynomials. In this paper we expand on these ideas and test this method extensively in solving various model problems. Of particular concern is to determine whether the advantages that may be gained by the reduction-to-periodicity method are offset by the extra computational time due to the additional $\log N$ factor in the operation count. From hereon we will refer to the reduction-to-periodicity method as the FFT method and will abbreviate the second-order finite difference method as the FD method.

The algorithmic formulation of the FFT method as well as the numerical procedures used for the solution of several model problems are described in Section 2. Section 3 summarizes the results for the model problems and provides direct comparisons between the FFT and FD methods. In Section 4 we give details of the fractional step method and the direct solution procedure used for the numerical integration of the two-dimensional time-dependent Navier–Stokes equations. The boundary/initial conditions for the velocity and pressure equations are also summarized. This section is also concerned with the driven cavity and backward-step problems and with direct comparisons between the FFT and FD methods. Finally, some concluding remarks are given in Section 5.

2. PROBLEM FORMULATION

An algorithmic formulation of the FFT technique and the time-stepping procedures used to solve several model equations are presented below.

2.1. The pseudospectral method

For a periodic function $F(x)$ which is specified by N values on equally spaced grid points,

$$x_n = n\Delta x, \quad n = 1, 2, \dots, N, \quad (1)$$

the corresponding values of the function $F_n \equiv F(x_n)$ may be expressed by the finite Fourier series

$$F_n = \sum_{l=1}^N f(k_l) \exp(ik_l x_n), \quad (2)$$

the inverse transform of which gives

$$f(k_l) = (1/N) \sum_{n=1}^N F_n \exp(-ik_l x_n), \quad k_l = 2\pi l/N\Delta x, \quad (3)$$

where k_l is the wave number along the x -direction. The pseudospectral approximation for the derivatives of F_n at each x_n can be obtained from equation (2) as

$$\partial F/\partial x_n = \sum_{l=1}^N [f(k_l)ik_l] \exp(ik_l x_n). \quad (4)$$

Since, at the boundaries, the convergence rate of this expansion depends on the boundary conditions (i.e. discontinuities of $F(x)$), we may subtract certain polynomial functions from $F(x)$ so that the residual will be a periodic function. Consequently, following the notation of

Reference 8, we can write

$$F(x) = F_p(x) + F_r(x), \quad (5)$$

where $F_p(x)$ and $F_r(x)$ correspond to polynomial and periodic parts of the function $F(x)$ respectively. From equation (4) the derivatives of $F(x)$ can be obtained as

$$\begin{aligned} F'(x) &= F'_p(x) + F'_r(x), \\ F''(x) &= F''_p(x) + F''_r(x). \end{aligned} \quad (6)$$

In this work we chose $F_p(x)$ as a fifth-order polynomial such that

$$F_p(x) = F(0) + a_1x + a_2x^2 + a_3x^3 + a_4x^4 + a_5x^5 \quad (7)$$

in the solution domain $0 \leq x \leq L$. The coefficients of this polynomial can be written in terms of the boundary values

$$\begin{aligned} D_0 &= F'(L) - F'(0), \\ D_1 &= F''(L) - F''(0), \\ D_2 &= F'''(L) - F'''(0), \\ D_3 &= F''''(L) - F''''(0), \\ D_4 &= F'''''(L) - F'''''(0), \end{aligned} \quad (8)$$

so that one obtains

$$\begin{aligned} a_5 &= (1/120L)D_4, \\ a_4 &= (1/24L)D_3 - \frac{5}{2}a_5L, \\ a_3 &= (1/6L)D_2 - 2a_4L - \frac{10}{3}a_5L^2, \\ a_2 &= (1/2L)D_1 - \frac{3}{2}a_3L - 2a_4L^2 - \frac{5}{2}a_5L^3, \\ a_1 &= (1/L)D_0 - a_2L - a_3L^2 - a_4L^3 - a_5L^4. \end{aligned} \quad (9)$$

With the choice of a fifth-order polynomial, the method formally becomes fifth-order accurate near the boundaries and sixth-order accurate in the interior.

An algorithm for the evaluation of the first and second derivatives of $F(x)$ can be written as follows.

- (1) Evaluate the derivatives of $F(x)$ at the boundaries either by one-sided differences or, if the function is known, directly from the function itself.
- (2) Calculate the coefficients a_1 – a_5 from equation (9).
- (3) Calculate the derivatives of the periodic part $F_r(x)$ from equations (3) and (4).
- (4) Calculate the derivatives of the polynomial part $F_p(x)$ by differentiating equation (7).
- (5) Finally, the first and second derivatives of $F(x)$ can be obtained from equation (6).

2.2. Time-stepping methods

The accuracy of the FFT method will be investigated by comparing the local relative error (defined as the difference between the exact solution to the problem and the numerical solution) of this scheme with a corresponding second-order accurate FD method in several convective–diffusive model problems. In particular, for extensions to multidimensional time-dependent fluid dynamics problems, we focus on second-order time discretization methods such as the Adams–Bashforth method, the Crank–Nicolson method and the compact Runge–Kutta

method. We also use the first-order Euler explicit method for comparison purposes. In order to summarize each of these methods, we will use a model equation of the form

$$\partial u/\partial t = G(u, x, t). \quad (10)$$

2.2.1. Adams–Bashforth method. The explicit second-order Adams–Bashforth method advances equation (10) in time according to

$$u^{n+1} = u^n + (\Delta t/2)[3G^n - G^{n-1}], \quad (11)$$

and for the first time step we can use

$$u^{n+1} = u^n + \Delta t G^n. \quad (12)$$

Note that owing to the weakly divergent amplification factor, $1 + O(\Delta t^2)$, this method is unconditionally unstable for the advection equation^{10,11} but becomes conditionally stable with the inclusion of a viscous term. Because the instability is weak, the method has been successfully used for long integration times in incompressible flow calculations.

2.2.2. Crank–Nicolson method. The Crank–Nicolson method is a second-order implicit scheme. This method advances equation (10) in time according to

$$u^{n+1} = u^n + (\Delta t/2)[G^{n+1} + G^n]. \quad (13)$$

Thus finding the solution at time step $n + 1$ requires the solution of a set of linear algebraic equations with a tridiagonal coefficient matrix. The method is unconditionally stable and therefore allows the use of much larger time steps than is possible with explicit methods. We use the Crank–Nicolson method in two-dimensional problems along directions in which the FFT method is not employed.

2.2.3. Compact Runge–Kutta method. A fully explicit, third-order, low-storage Runge–Kutta method was given by Williamson.¹² The algorithm reads

$$\begin{aligned} H_1 &= \Delta t G_n, \\ u_1 &= u_0 + \frac{1}{3}H_1, \\ H_2 &= \Delta t G_1 - \frac{5}{9}H_1, \\ u_2 &= u_1 + \frac{15}{16}H_2, \\ H_3 &= \Delta t G_2 - \frac{153}{128}H_2, \\ u^{n+1} &= u_2 + \frac{8}{15}H_3. \end{aligned} \quad (14)$$

This high-order, low-storage scheme requires two arrays per variable and could be used either to increase the accuracy of the integration or to allow a larger time step. For convective problems the scheme is found to be stable for Courant numbers $CN \leq 0.2$.¹³

3. DISCUSSION OF RESULTS FOR MODEL PROBLEMS

In this section a discussion of the results for several model problems is presented. The accuracy of the results for a solution function F is defined in terms of the local relative error

$$\varepsilon_{\text{rel}} = (F_{\text{analytical}} - F_{\text{computed}})/F_{\text{analytical}}. \quad (15)$$

3.1. Simple function derivatives

In the first example we use a damped sine wave function⁷ to investigate the accuracy of the FFT method in evaluating function derivatives. In particular we consider a function given by

$$F(x) = e^{ax} \sin(2\pi bx), \tag{16}$$

with $a = -2$, $b = \frac{3}{4}$ and $0 \leq x \leq 1$. From equation (16) expressions for $F'(x)$ and $F''(x)$ can be

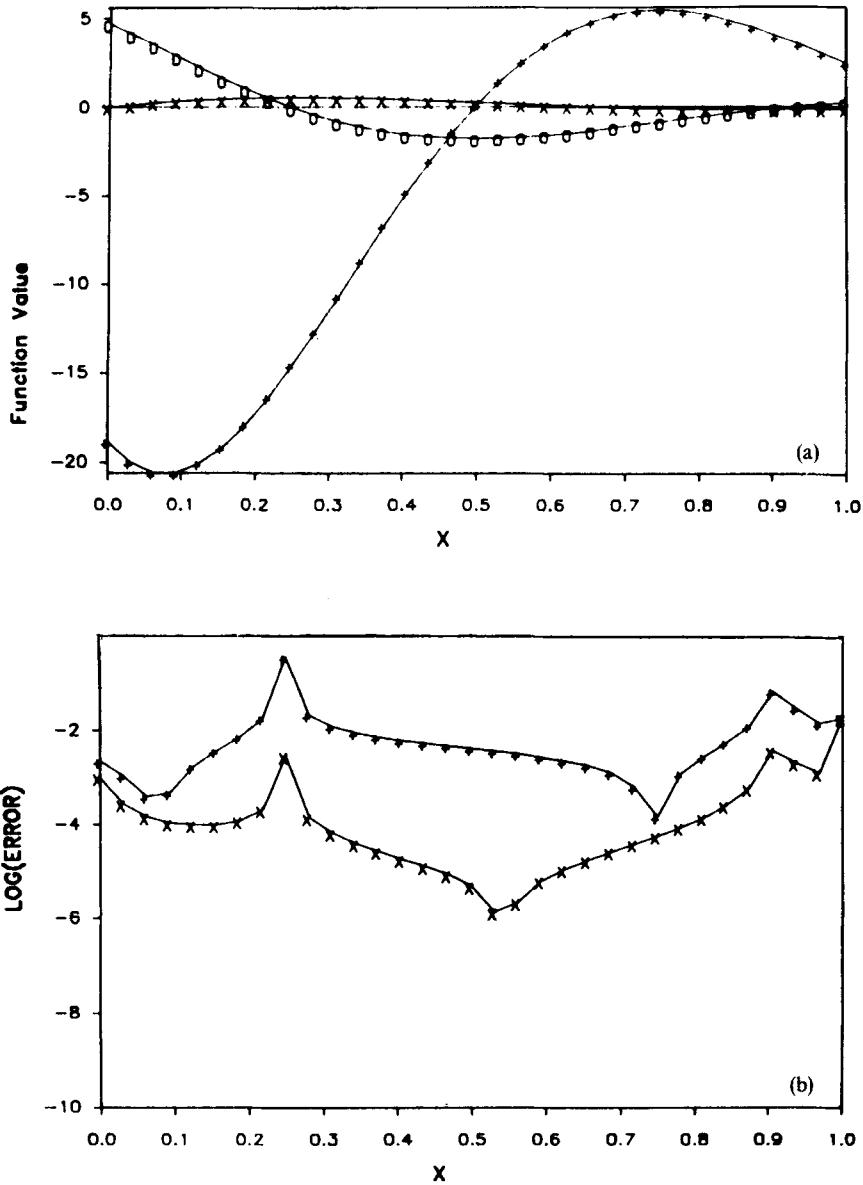


Figure 1. (a, b)

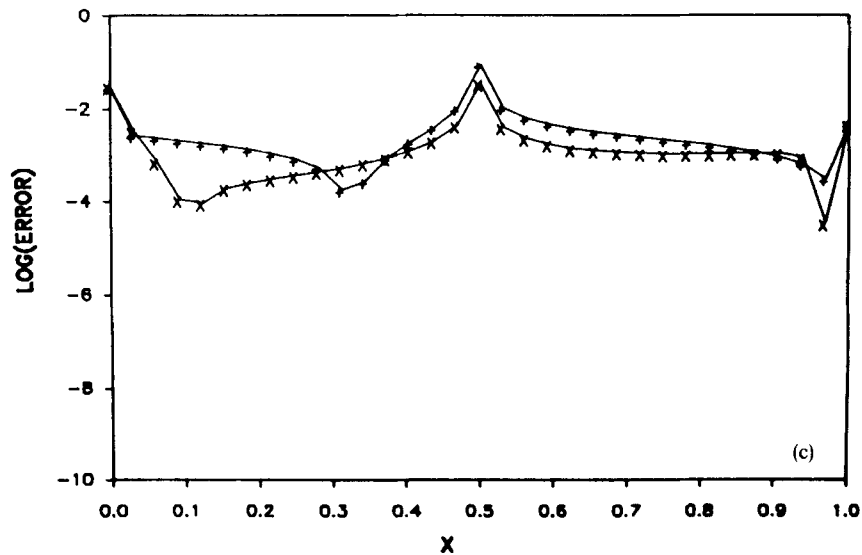


Figure 1. Solution profiles of the damped sine function: (a) exact function (\times), first derivative (\circ), second derivative ($+$); (b) local relative errors for the first derivative, FFT (\times), FDM ($+$); (c) local relative errors for the second derivative, FFT (\times), FDM ($+$) (33 mesh)

derived as

$$F'(x) = e^{ax} [a \sin(2\pi bx) + 2\pi b \cos(2\pi bx)]$$

$$F''(x) = 4\pi ab e^{ax} \cos(2\pi bx) + e^{ax}(a^2 - 4\pi^2 b^2) \sin(2\pi bx). \quad (17)$$

Figure 1(a) shows the exact results for the function itself and its first and second derivatives. In Figure 1(b) the local relative errors for the FFT and FD methods are compared. As evident from this figure, the FFT method decreases $|\epsilon_{rel}|$ by about three orders of magnitude in the region $0.35 < x < 0.65$ and provides some improvement over the FD method when $x \rightarrow 0$ and $x \rightarrow 1$, i.e. close to the boundaries, where the accuracy of the FFT method should be expected to decrease. However, for the second derivative, Figure 1(c), the FFT method yields only marginal improvement for most of the solution domain. In a similar test problem, the improvement of accuracy obtained by the FFT method was found to remain several orders of magnitude less than a corresponding true spectral method using Chebyshev polynomials with the same number of collocation points.⁸

3.2. One-dimensional diffusion equation

Consider the unsteady one-dimensional heat conduction problem for which the governing equation reads

$$\frac{\partial T}{\partial t} = \alpha^2 \frac{\partial^2 T}{\partial x^2}, \quad 0 \leq x \leq \pi. \quad (18)$$

The initial conditions are given as

$$T = 0, \quad t = 0, \quad x < 1,$$

$$T = 1, \quad t = 0, \quad x = \pi, \quad (19)$$

with the boundary conditions

$$\begin{aligned} T &= 0, & t > 0, & x = 0, \\ T &= 1, & t > 0, & x = \pi. \end{aligned} \tag{20}$$

The exact solution for this problem reads

$$T(x,t) = x + \sum_1^{\infty} (-1)^n (2/n\pi) \sin(n\pi x) \exp(-n^2\pi^2\alpha^2 t). \tag{21}$$

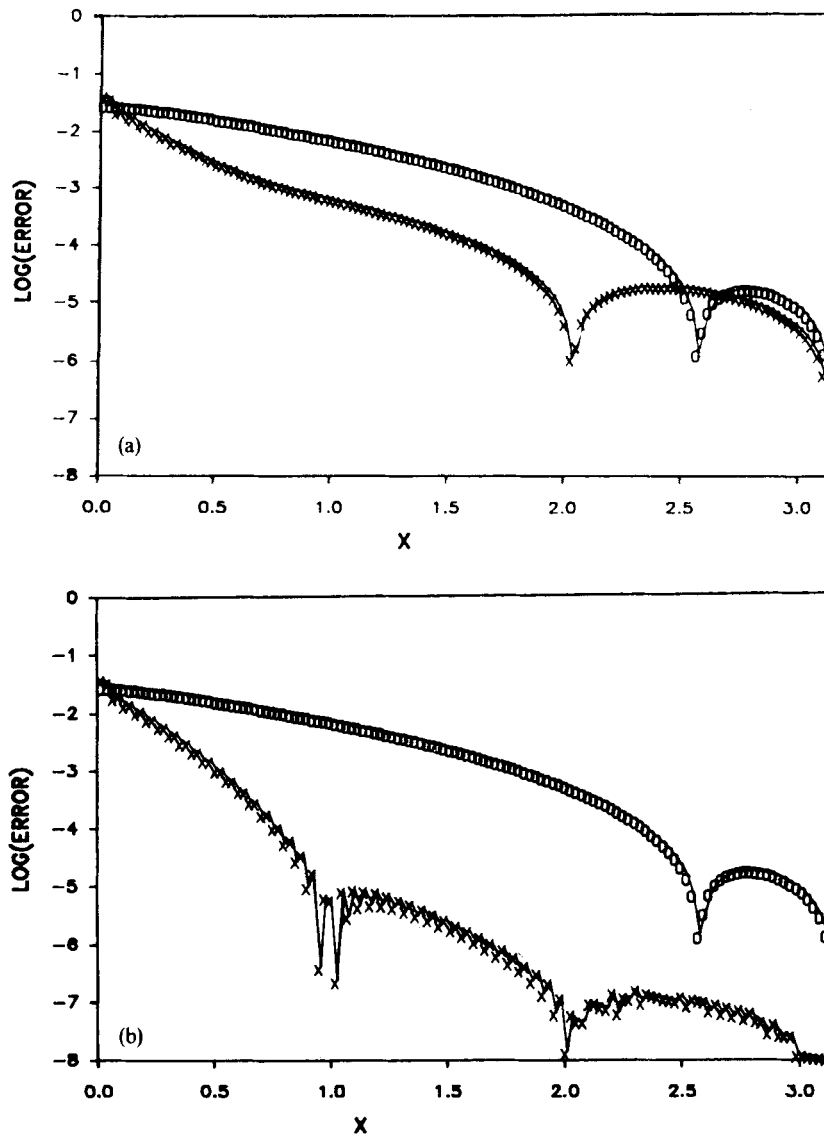


Figure 2. Local relative errors for the solutions of the 1D diffusion equation at $t = 200\,000$: FFT (\times); FDM (\circ); (a) Euler explicit scheme; (b) compact low-storage Runge-Kutta scheme (129 mesh)

Note that with the high-order polynomials, the FFT method requires an explicit numerical scheme for time discretization. For simplicity we use the Euler explicit scheme

$$T^{n+1} = T^n + \alpha^2 \Delta t (\partial^2 T / \partial x^2)^n. \quad (22)$$

In Figure 2(a) results are presented at $t = 200\,000$ indicating improved accuracy for the FFT method over most of the solution domain up to two orders of magnitude. Further improvement in accuracy is obtained by the use of the compact Runge–Kutta method, as shown in Figure 2(b). Accordingly, an error decrease of several orders of magnitude is obtained by the FFT method as compared to Euler time advancement, whereas the FD method is almost invariant to time discretization.

3.3. One-dimensional convective–diffusion equation

The one-dimensional non-linear convective–diffusion equation is given as

$$\frac{\partial u}{\partial t} + u \frac{\partial u}{\partial x} = v \frac{\partial^2 u}{\partial x^2}, \quad (23)$$

with v as the kinematic viscosity. This equation is known as the one-dimensional non-linear Burger's equation. An exact solution for $v = 1$, given Reference 14, will be considered. This reads

$$u(x, t) = \frac{-2 \sinh(x)}{\cosh(x) - e^{-t}}. \quad (24)$$

For the computational domain $-6 \leq x \leq 6$ we prescribe the initial conditions as

$$\begin{aligned} u &= 2, & t &= 0, & x &= -6, \\ u &= -2, & t &= 0, & x &= 6, \end{aligned} \quad (25)$$

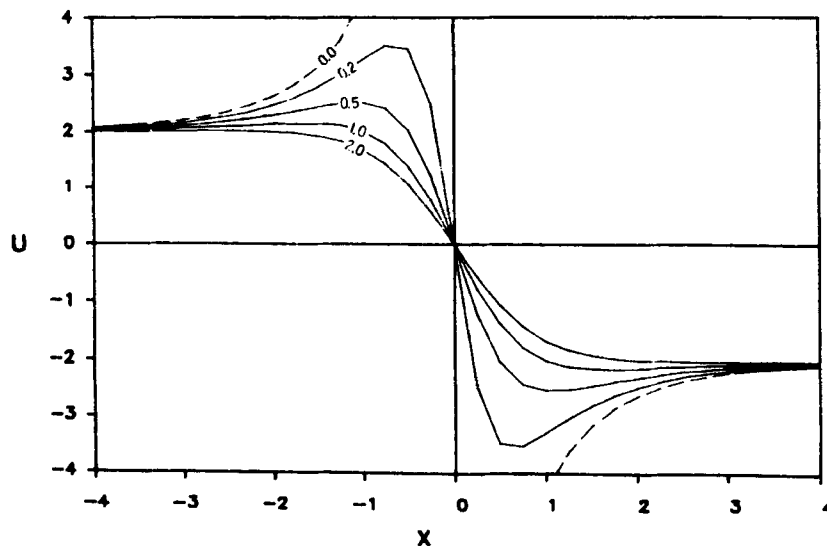


Figure 3. Exact solutions of the 1D Burger's equation at different time levels

and the time-dependent boundary conditions are

$$\begin{aligned}
 u &= \frac{-2 \sinh(-6)}{\cosh(-6) - e^{-t}}, & t > 0, & \quad x = -6, \\
 u &= \frac{-2 \sinh(6)}{\cosh(6) - e^{-t}}, & t > 0, & \quad x = 6.
 \end{aligned}
 \tag{26}$$

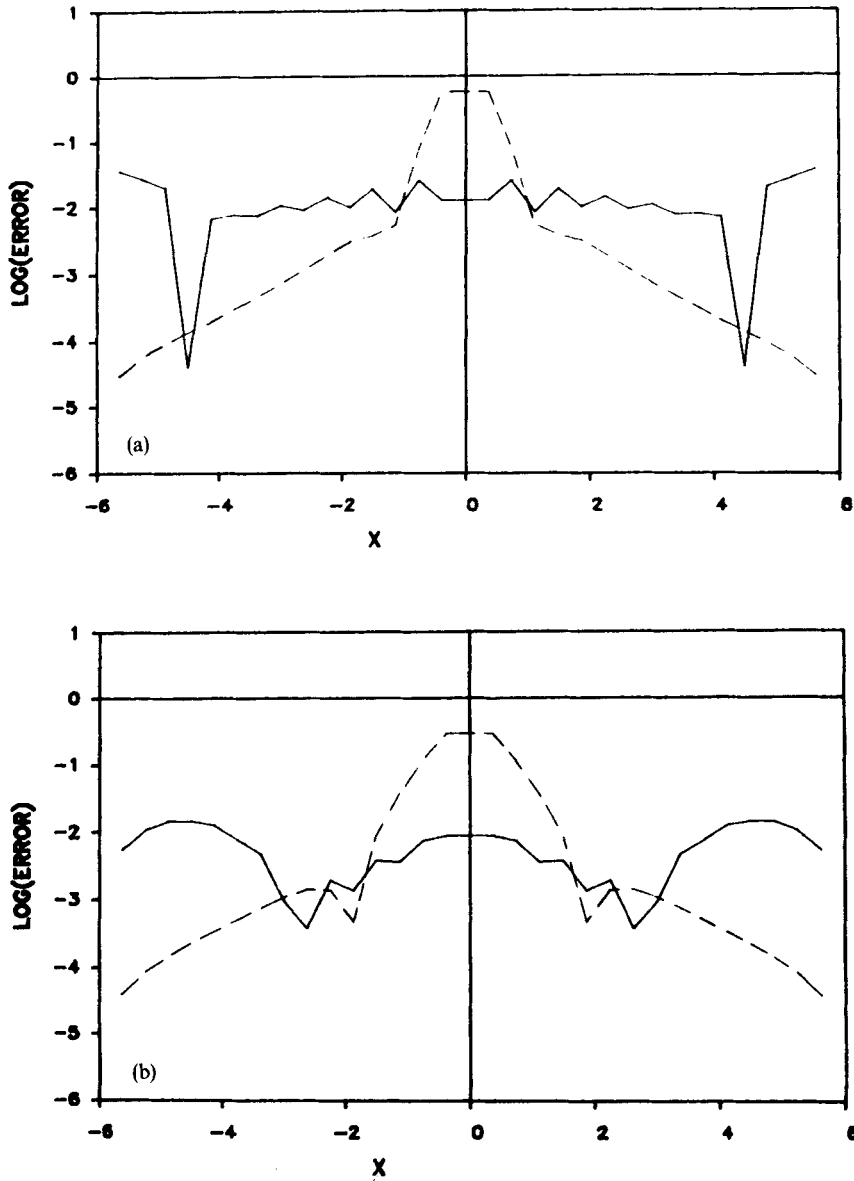


Figure 4. (a, b)

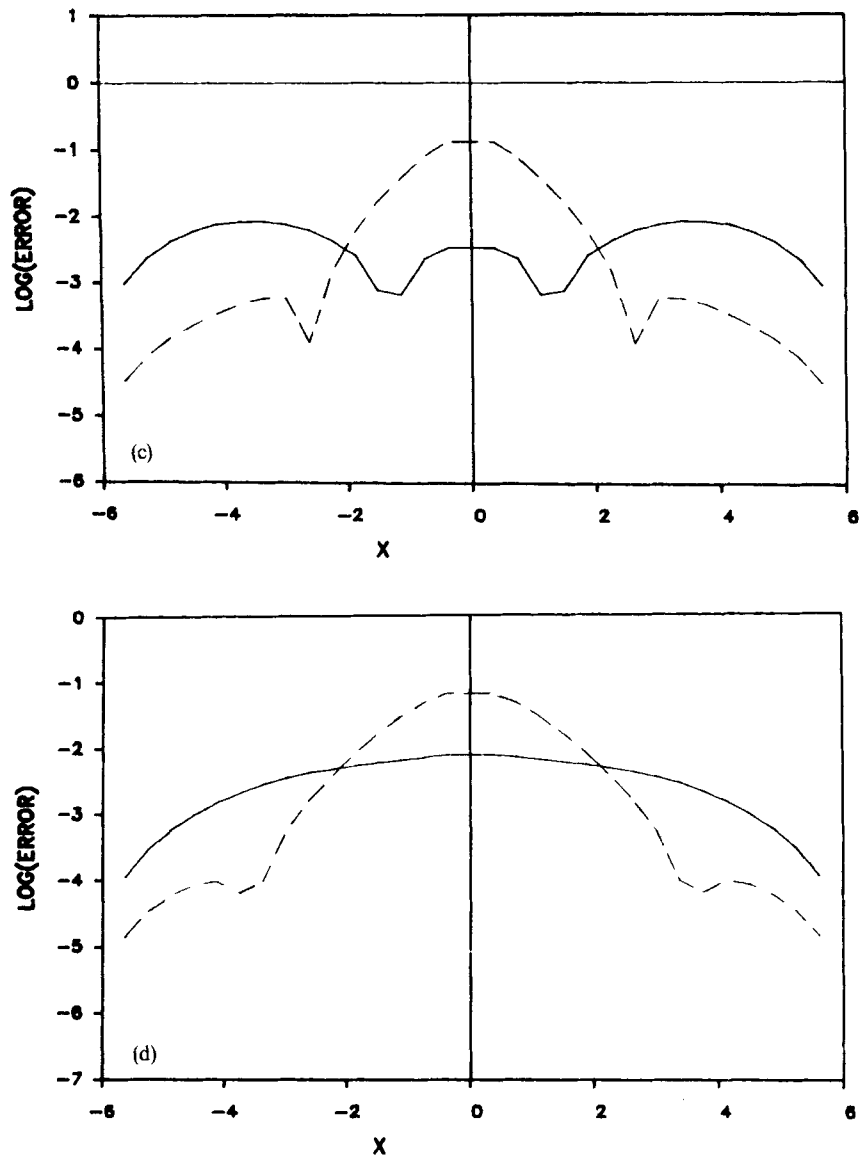


Figure 4. Relative errors for the solution of the 1D Burger's equation using the Adams-Bashforth method in both the convective and diffusion terms: (a) $t = 0.2$; (b) $t = 0.5$; (c) $t = 1.0$; (d) $t = 2.0$ (33 mesh); —, FFT; ---, FDM

Figure 3 presents the closed-form solutions. The numerical solutions were obtained by applying the Adams-Bashforth scheme to both the convective and diffusion terms. Results for the FFT and FD methods are shown in Figures 4 and 5 at different times, using 33 and 129 grid points respectively; as expected, for both methods improved accuracy is obtained with increasing grid points. This mesh refinement study provides some estimates of the cost of increasing accuracy for the FFT method. First, a comparison of Figures 4(a-d) with the corresponding Figures 5(a-d) illustrates that the FD method displays an error decrease by a factor of N^{-2} in accordance with its

second-order formal accuracy. The error decrease that is shown by the FFT method varies between roughly N^{-1} ($t = 0.5$) and $N^{-7/2}$ ($t = 2.0$), approaching the error decrease of a fourth-order finite difference method. However, since the cost of a fourth-order finite difference second derivative will be about 3.0 (for a 32 mesh) to 4.5 (for a 128 mesh) times less expensive than the FFT method, the accuracy gained by the FFT method at large integration times does not seem to be cost-efficient for this problem.

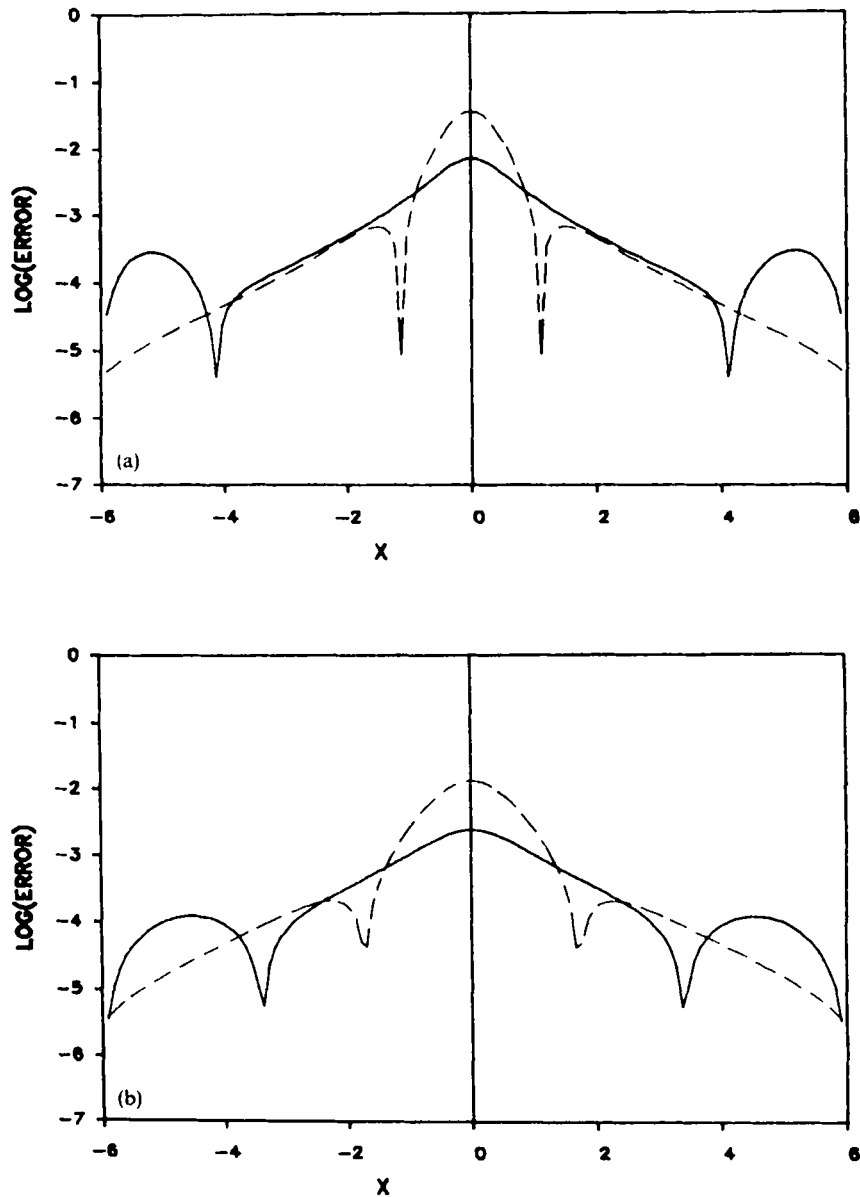


Figure 5. (a, b)

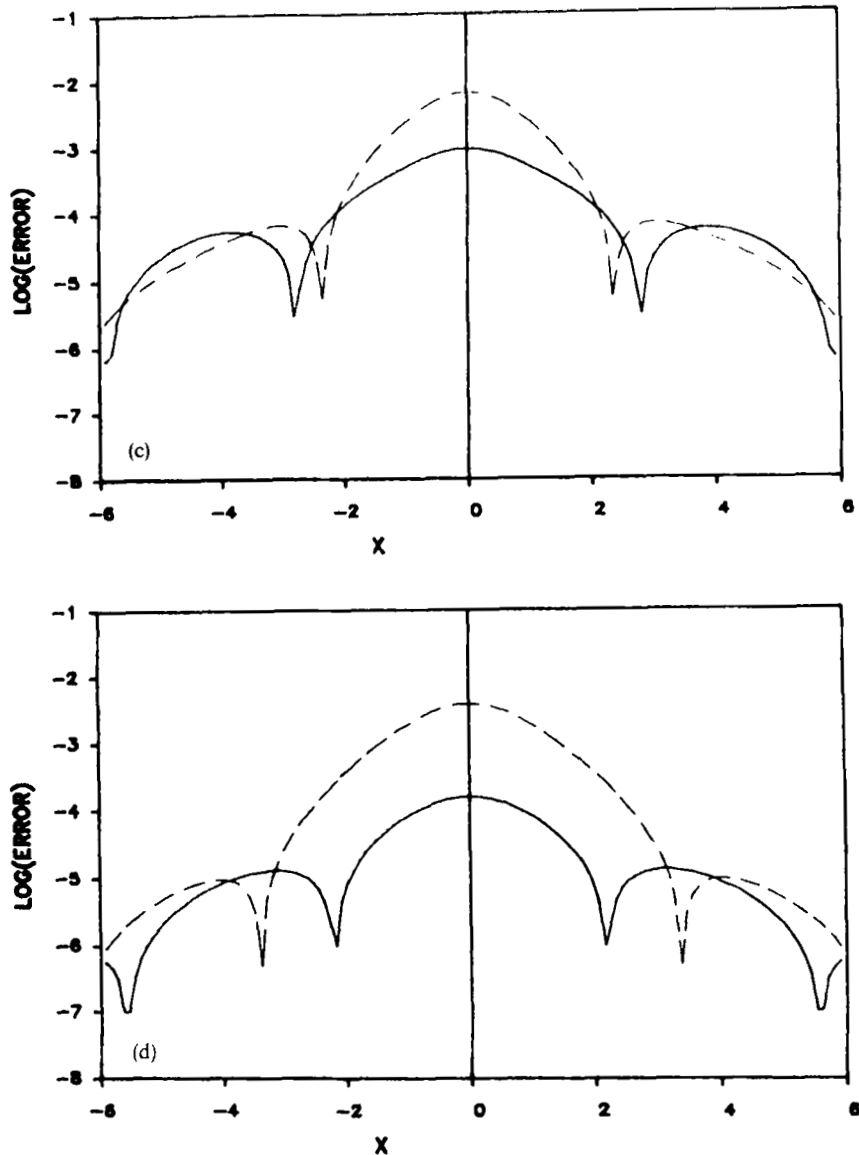


Figure 5. Relative errors with the same computational scheme as in Figure 4: (a) $t = 0.2$; (b) $t = 0.5$; (c) $t = 1.0$; (d) $t = 2.0$ (129 mesh); ---, FFT; —, FDM

We investigated the influence of time discretization on solution accuracy of the FFT method by implementing several procedures to solve this strongly diffusive problem using 129 grid points. Figure 6 shows results for three types of time-stepping techniques at various times using only the FFT method. The techniques we used are: (i) Euler explicit (EE) on both the convective and diffusion terms; (ii) Adams–Bashforth (AB) on the convective terms and EE on the diffusion term; and (iii) compact Runge–Kutta (RK) on the convective term and EE on the diffusion term. It is obvious from these figures that all the methods considered have the same relative error except at

later times, i.e. at $t = 2$, where scheme (ii) provides slightly improved accuracy in the central region of the solution domain. Consequently, this time discretization study leads to the idea that significant improvement in solution accuracy will not be gained via time-stepping procedures for the convection-diffusion equation.

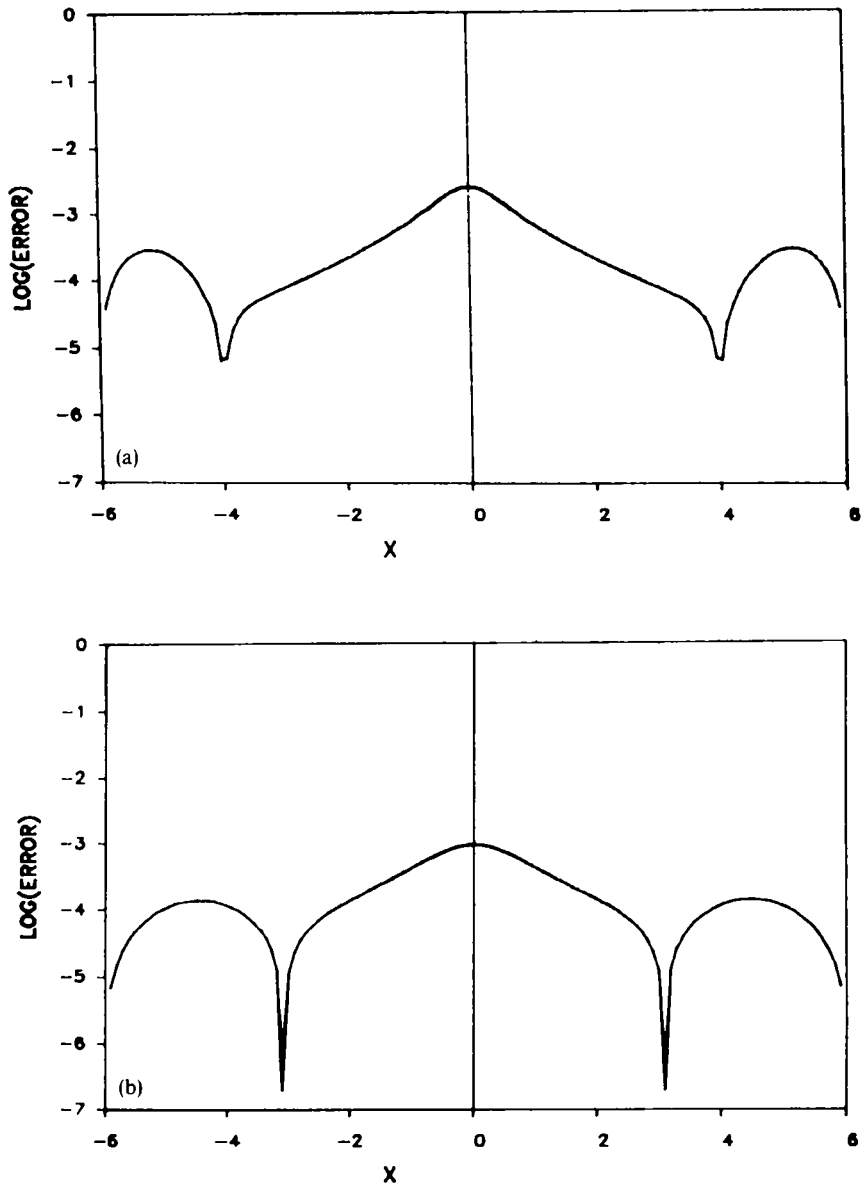


Figure 6. (a, b)

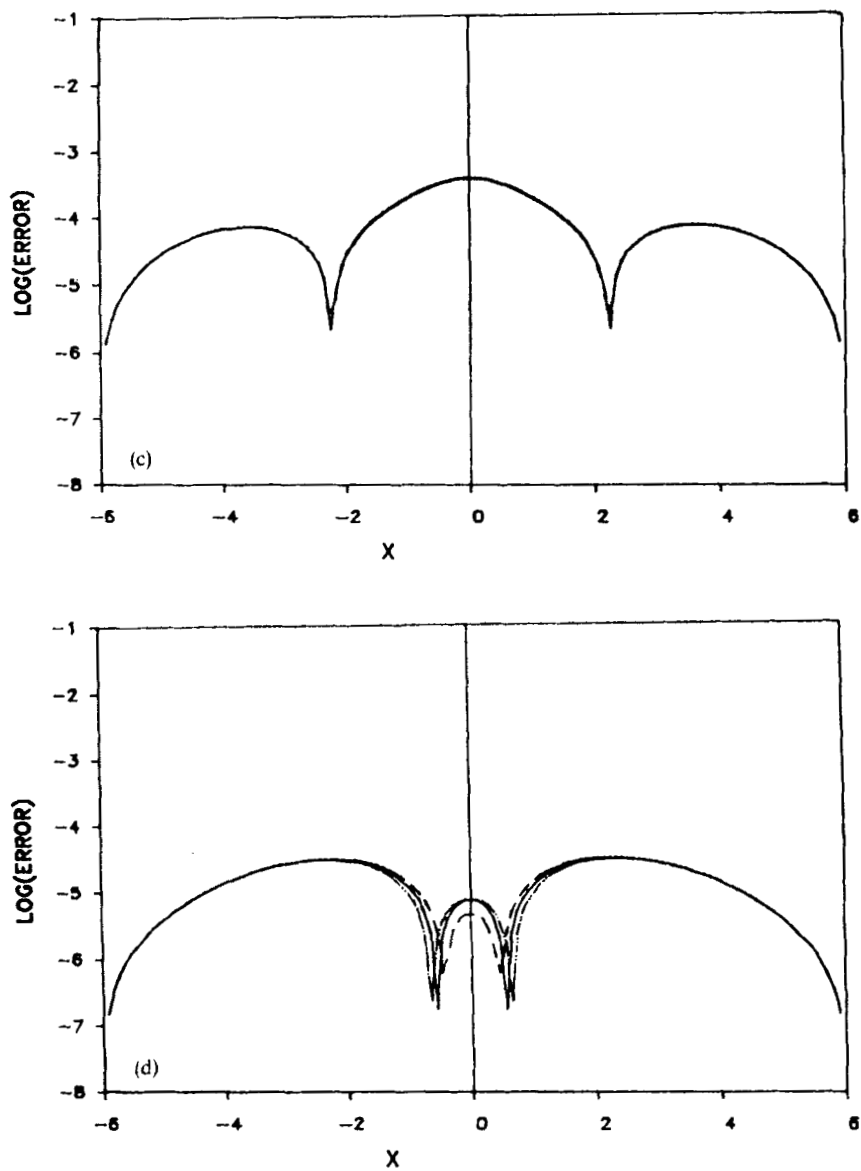


Figure 6. Relative error for various schemes for the solution of the 1D Burger's equation with FFT method: (a) $t = 0.2$; (b) $t = 0.5$; (c) $t = 1.0$; (d) $t = 2.0$ (129 mesh); —, (i); ---, (ii); - · - ·, (iii) as described in the text

3.4. Two-dimensional diffusion equation

In this section we extend the test problems to two-dimensional domains and consider the diffusion equation

$$\frac{\partial T}{\partial t} = v \left(\frac{\partial^2 T}{\partial x^2} + \frac{\partial^2 T}{\partial y^2} \right). \quad (27)$$

We investigate the model problem given in Reference 15 in the domain $0 \leq x \leq 1$ and $0 \leq y < \infty$, for which the initial condition is

$$T(x, y, 0) = \sin(2\pi x) \exp(-y^2). \tag{28}$$

The time-dependent boundary conditions are

$$\begin{aligned} T(x, \infty, t) &= 0, \\ T(x, 0, t) &= \sin(2\pi x) \frac{\exp(-4\pi^2 vt)}{\sqrt{1 + 4vt}}, \\ T(0, y, t) &= 0, \\ T(1, y, t) &= 0. \end{aligned} \tag{29}$$

The analytical solution for this problem is

$$T(x, y, t) = \sin(2\pi x) \frac{\exp(-4\pi^2 vt)}{\sqrt{1 + 4vt}} \exp\left(\frac{-y^2}{1 + 4vt}\right). \tag{30}$$

In this problem, second-order central differences are used along the y -direction and, owing to steep gradients along this co-ordinate, we use a stretching function of the form

$$y_j = \Delta y \left[\frac{j-1}{N-j} \right], \tag{31}$$

where y_j is defined as the y -co-ordinate at the j th grid point of the total N grid points, and Δy is the first interval at the boundary. Along the x -direction we implement either the FFT method or the FD method.

The exact solution at $t = 0.5$ is shown in Figure 7, while Figures 8–10 display the results using different schemes, all of which were computed with $\Delta t = 0.0005$. It can be observed that the Adams–Bashforth method (Figure 8) reduces the local accuracy when it is employed for the diffusion terms. It is also interesting to note that the Euler explicit method applied in both the streamwise and spanwise directions (Figure 9) is the most accurate scheme for this two-dimensional diffusion equation when used with the FFT scheme. For wall-bounded problems,

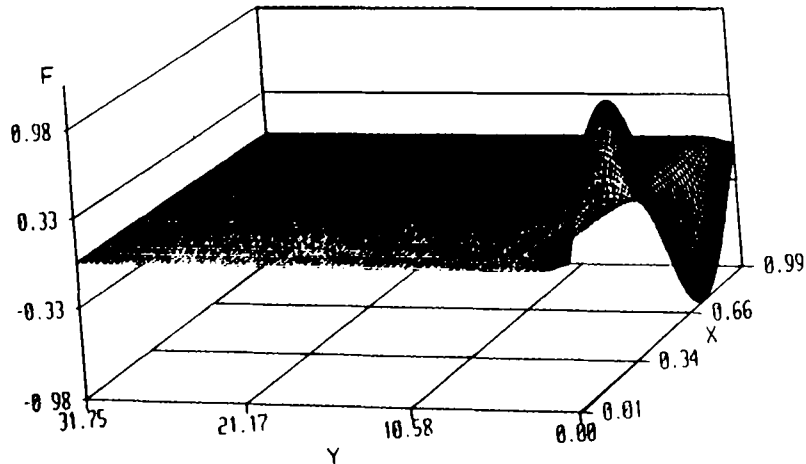


Figure 7. Exact solution of the 2D diffusion equation at $t = 0.5$ (129×129 mesh)

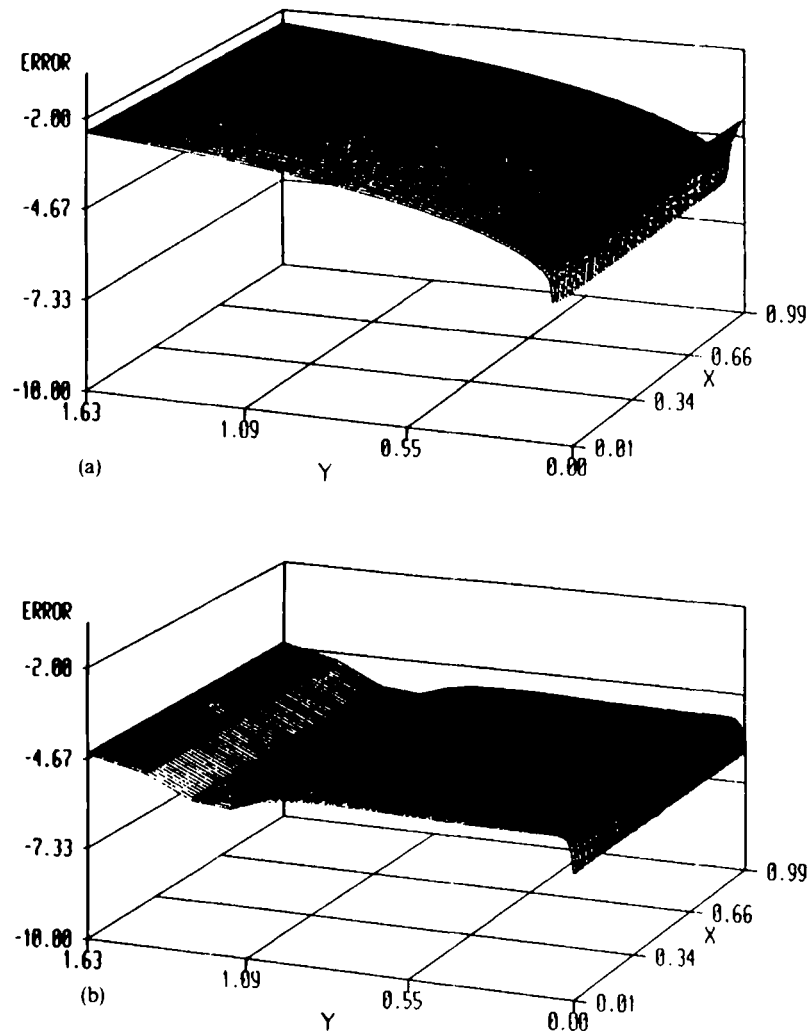


Figure 8. Relative errors (log error) for the 2D diffusion equation at $t = 0.5$ using the Adams–Bashforth method in both diffusion directions: (a) FFT; (b) FDM (129×129 mesh)

strong viscous effects along directions perpendicular to the wall impose very stiff limitations on allowable Δt in explicit methods. For such problems, the implicit Crank–Nicolson method (Figure 10) will be more advantageous. In all the cases, both methods indicate roughly comparable accuracy and no significant error attenuation is indicated by the FFT method in comparison with the FD method.

4. NAVIER–STOKES SOLUTIONS

In the preceding section the FFT technique was used to numerically integrate several convective–diffusive problems and, in general, provides comparable accuracy with a second-order

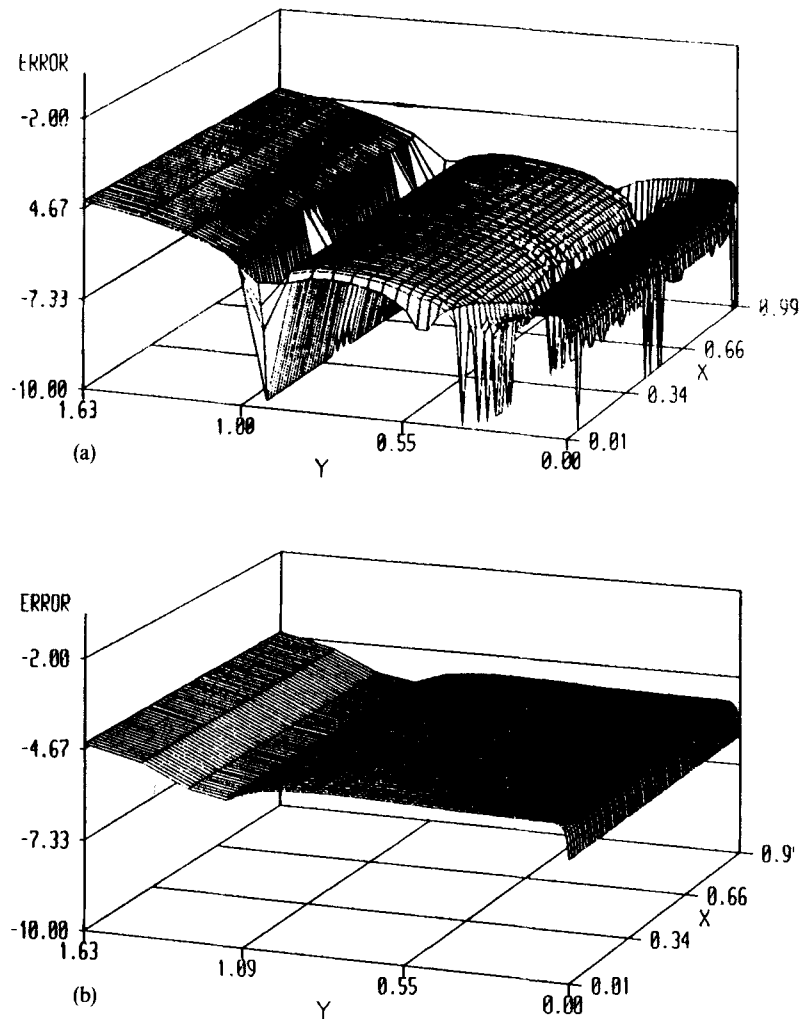


Figure 9. Relative errors (log error) for the 2D diffusion equation at $t = 0.5$ using the Euler explicit method in both directions: (a) FFT; (b) FDM (129×129 mesh)

finite-difference method. In this section we use this method for the solution of the two-dimensional, time-dependent, incompressible Navier–Stokes equations. We consider the driven cavity flow and the backward-facing step as model problems. For these problems the x -directional derivatives are computed by either the FFT or the FD method with non-periodic inflow/outflow or no-slip boundary conditions. The y -directional derivatives are always discretized by the FD method.

We consider the two-dimensional, incompressible, time-dependent Navier–Stokes and the continuity equations non-dimensionalized by the characteristic length and velocity scales, L and U_0 , respectively:

$$\frac{\partial u_i}{\partial t} = -\frac{\partial}{\partial x_j}(u_i u_j) - \frac{\partial P}{\partial x_i} + \frac{1}{Re} \frac{\partial^2 u_i}{\partial x_j^2}, \quad (32)$$

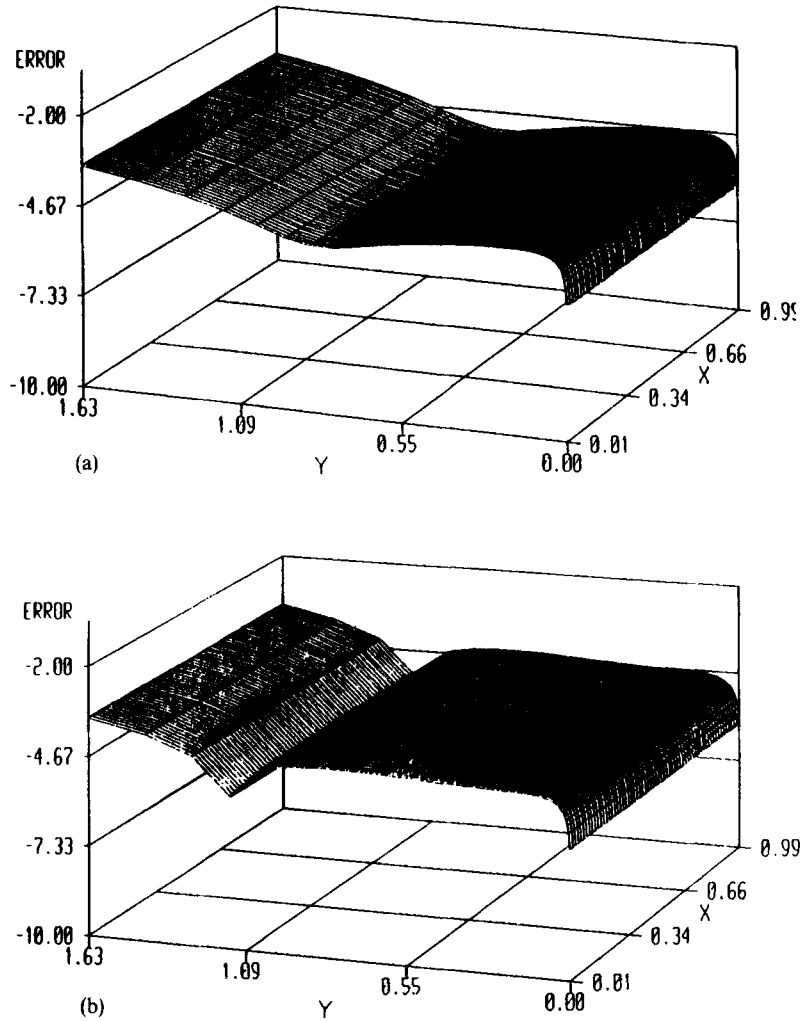


Figure 10. Relative errors (log error) for the 2D diffusion equation at $t = 0.5$ using the Euler explicit method in streamwise and the Crank–Nicolson method in cross-stream directions: (a) FFT; (b) FDM (129×129 mesh)

$$\frac{\partial u_i}{\partial x_i} = 0. \tag{33}$$

We define

$$L_i = -\frac{\partial}{\partial x_j}(u_i u_j) \quad \text{and} \quad Re = \frac{U_0 L}{\nu}. \tag{34}$$

We implement the second-order explicit Adams–Bashforth scheme for the convective terms, the Euler explicit method for the streamwise (x) diffusion term and the second-order implicit Crank–Nicolson method for the cross-stream (y) diffusion term. Using the fractional step method,^{16,17} we write the first step for the intermediate quantity \tilde{u}_i :

$$\frac{\tilde{u}_i - u_i^n}{\Delta t} = \frac{3}{2}L_i^n - \frac{1}{2}L_i^{n-1} + \frac{1}{Re} \frac{\partial^2 u_i^n}{\partial x_1 \partial x_1} + \frac{1}{2Re} \frac{\partial^2 \tilde{u}_i}{\partial x_2 \partial x_2} + \frac{1}{2Re} \frac{\partial^2 u_i^n}{\partial x_2 \partial x_2}, \tag{35}$$

from which one obtains

$$-\frac{\Delta t}{2Re} \frac{\partial^2 \tilde{u}_i}{\partial x_2 \partial x_2} + \tilde{u}_i = u_i^n + \frac{\Delta t}{2}(3L_i^n - L_i^{n-1}) + \frac{\Delta t}{Re} \frac{\partial^2 u_i^n}{\partial x_1 \partial x_1} + \frac{\Delta t}{2Re} \frac{\partial^2 u_i^n}{\partial x_2 \partial x_2} \equiv \text{RHS}_i^n. \quad (36)$$

We can now apply the FD method to evaluate the second derivative for the cross-stream diffusion term:

$$\tilde{u}_i - \frac{\Delta t}{2Re(\Delta y)^2}(\tilde{u}_{i+1} - 2\tilde{u}_i + \tilde{u}_{i-1}) = \text{RHS}_i^n. \quad (37)$$

The above tridiagonal equation can be solved efficiently for the quantity \tilde{u}_i . By inspecting the original equation (32), we can also obtain the expression

$$\frac{u_i^{n+1} - u_i^n}{\Delta t} = \frac{3}{2}L_i^n - \frac{1}{2}L_i^{n-1} + \frac{1}{Re} \frac{\partial^2 u_i^n}{\partial x_1 \partial x_1} + \frac{1}{2Re} \frac{\partial^2 u_i^{n+1}}{\partial x_2 \partial x_2} + \frac{1}{2Re} \frac{\partial^2 u_i^n}{\partial x_2 \partial x_2} - \frac{\partial P^{n+1}}{\partial x_i}. \quad (38)$$

Subtracting equation (35) from (38) yields

$$\frac{u_i^{n+1} - \tilde{u}_i}{\Delta t} = \frac{1}{2Re} \left(\frac{\partial^2 u_i^{n+1}}{\partial x_2 \partial x_2} - \frac{\partial^2 \tilde{u}_i}{\partial x_2 \partial x_2} \right) - \frac{\partial P^{n+1}}{\partial x_i} \equiv -\frac{\partial \Phi^{n+1}}{\partial x_i}. \quad (39)$$

Taking the divergence of both sides of equation (39), we obtain

$$\frac{\nabla \cdot u_i^{n+1} - \nabla \cdot \tilde{u}_i}{\Delta t} = -\nabla^2 \Phi^{n+1}. \quad (40)$$

After enforcing the continuity equation, i.e.

$$\nabla \cdot u_i^{n+1} = 0, \quad (41)$$

equation (40) gives

$$\frac{\nabla \cdot \tilde{u}_i}{\Delta t} = \nabla^2 \Phi^{n+1}. \quad (42)$$

From (42) we can solve for Φ^{n+1} ; then using $(\partial\Phi/\partial x_i)^{n+1}$ in equation (39), u_i^{n+1} is obtained. The spatial discretization is done on a staggered grid following Harlow and Welch,¹⁸ a schematic diagram is given in Figure 11.

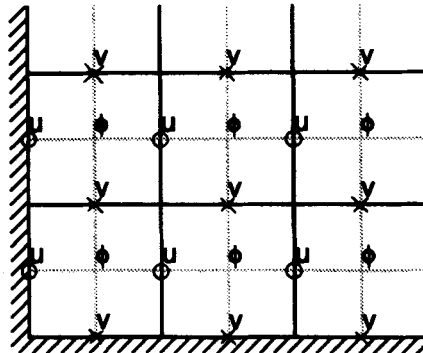


Figure 11. Schematic diagram of the staggered grid

At the solid walls, boundary conditions for the velocities parallel to the walls are obtained using averaging, which results in

$$v_0 = 2v_\tau - v_1. \quad (43)$$

It is also possible to use a higher-order one-sided derivative at this boundary which can be written as

$$v_0 = \frac{1}{3}(v_2 - 6v_1 + 8v_\tau). \quad (44)$$

In equations (43) and (44), v_1 and v_2 are the interior velocities and v_τ is the wall velocity (Figure 12). Boundary conditions for the velocities normal to the wall can then be obtained by satisfying continuity on the wall cell shown in Figure 13. For a stationary wall this gives

$$u_0 = u_1. \quad (45)$$

Boundary conditions for Φ follow directly from the normal momentum equation evaluated at the boundaries. The intermediate boundary conditions for velocities with $O(\Delta t^2)$ accuracy can be obtained following the analysis of Kim and Moin¹⁷ as

$$\tilde{u}_i = u_i^{n+1} + \Delta t \partial \phi^n / \partial x_i. \quad (46)$$

It is interesting to note that even the zeroth-order boundary condition, $\tilde{u}_i = u_i^{n+1}$, provides a consistent scheme for the test problems considered in this work. Finally, the inflow/outflow boundary conditions of the back-step problem using the FFT method require the evaluation of the product term $\partial(uv)/\partial x$ at the v -nodes. This was done by bilinear interpolation of u at the interior cells and by satisfying continuity on the boundaries.

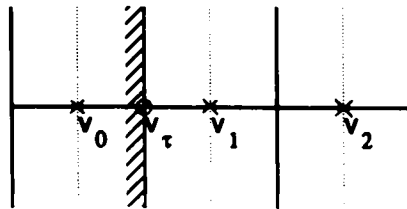


Figure 12. Boundary conditions for the v -velocity

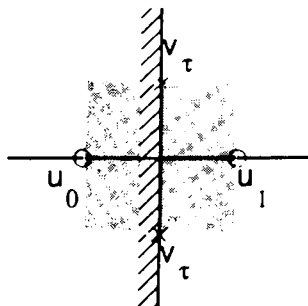


Figure 13. Boundary conditions for the u -velocity

The solution of the Poisson equation for Φ was obtained by using a direct band solver for the five-point finite difference operator. For this purpose we used the IMSL subroutines LUDAPB and LUREPB on the VAXG system and the NASA/Langley library subroutine Q4BAND on the VPS32 vector processor. Since the coefficient matrix is constant, the LU decomposition is done only at the first time step, resulting in substantial savings in CPU time. The feasibility of this direct solution procedure for moderate-size systems has been documented in References 19 and 20.

In the remainder of this section we present a direct comparison of the FD and FFT methods when they are used to evaluate the x -directional derivatives in the fractional step procedure outlined above. As model problems, we consider the shear-driven cavity and the back-facing step; note that owing to the existence of solid walls along the x -direction, the shear-driven cavity presents a very stiff test case for the FFT method.

4.1. Flow in a driven cavity

The first test case for the comparison of the FD and FFT methods is the shear-driven cavity, the geometry and boundary conditions of which are given in Figure 14. Note that the flow is driven by the downward motion of the right-hand wall. Once the motion occurs, a primary vortex is formed near the centre region of the cavity. At $Re = 1$ the flow is almost symmetric with respect to the centreline. As the Reynolds number increases, the vortex centre moves towards the right lower corner, and with further increase in Reynolds number it moves back towards the cavity centre. In

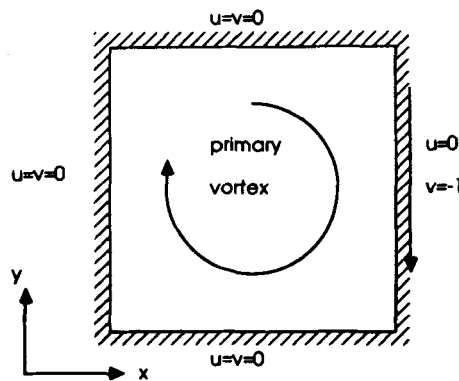


Figure 14. Geometry of the driven cavity problem

Table I. Streamfunction at centre of primary vortex for different Reynolds numbers

Re	Present FFT	Present FD	Ref. 17	Ref. 21	Ref. 22
1	-0.0991	-0.099	-0.099	—	-0.100
(mesh)	33×33	33×33	65×65		121×121
100	-0.102	-0.102	-0.103	-0.103	-0.103
(mesh)	33×33	33×33	65×65	129×129	121×121
400	-0.109	-0.107	-0.112	-0.114	-0.113
(mesh)	33×33	33×33	65×65	257×257	141×141
1000	-0.105	-0.102	-0.116	-0.118	-0.116
(mesh)	33×33	33×33	97×97	129×129	141×141

Table I we list the values of the streamfunction (obtained by integrating the calculated velocity field) at the centre of the primary vortex for various Reynolds numbers. The present results are compared with those of References 17, 21 and 22 and remain within a few percent of these high-resolution computations up to $Re = 400$ in spite of the lower resolution (and no mesh stretching) employed in this work. At $Re = 1000$ the effect of low mesh resolution becomes pronounced and the value of the streamfunction at the vortex centre diverges from the high-resolution simulations. For this quantity the improvement gained by the FFT method is only marginal, e.g. one obtains a typical relative error of 9.5% for the FFT method compared with 12.1% for the FD method.

In Figures 15 and 16 we present streamfunction contours at several values of the Reynolds number for the FD and FFT methods respectively. For both sets of results the locations of the

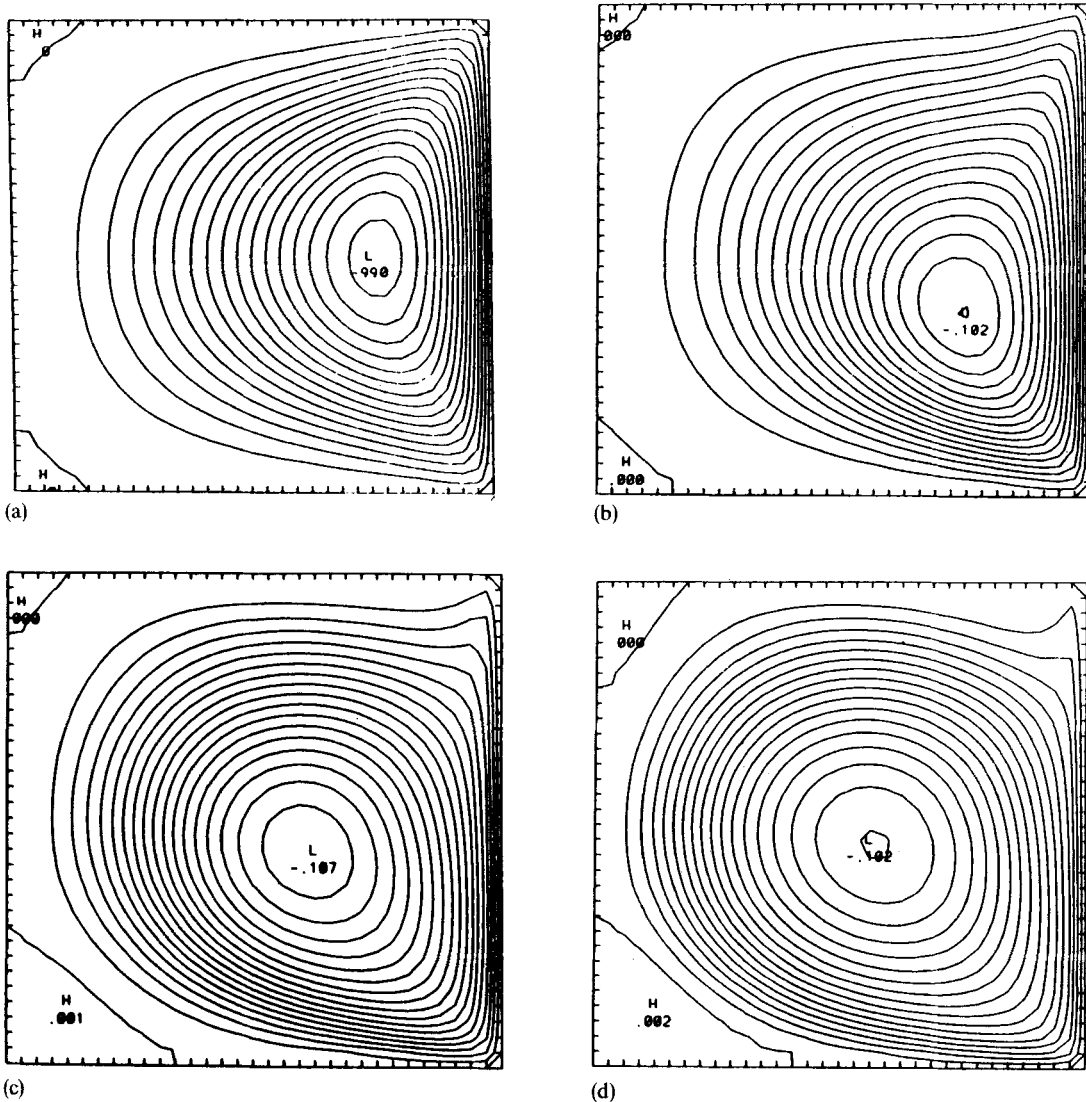


Figure 15. Streamfunction contours for the driven cavity problem, FDM results: (a) $Re = 1$; (b) $Re = 100$; (c) $Re = 400$; (d) $Re = 1000$

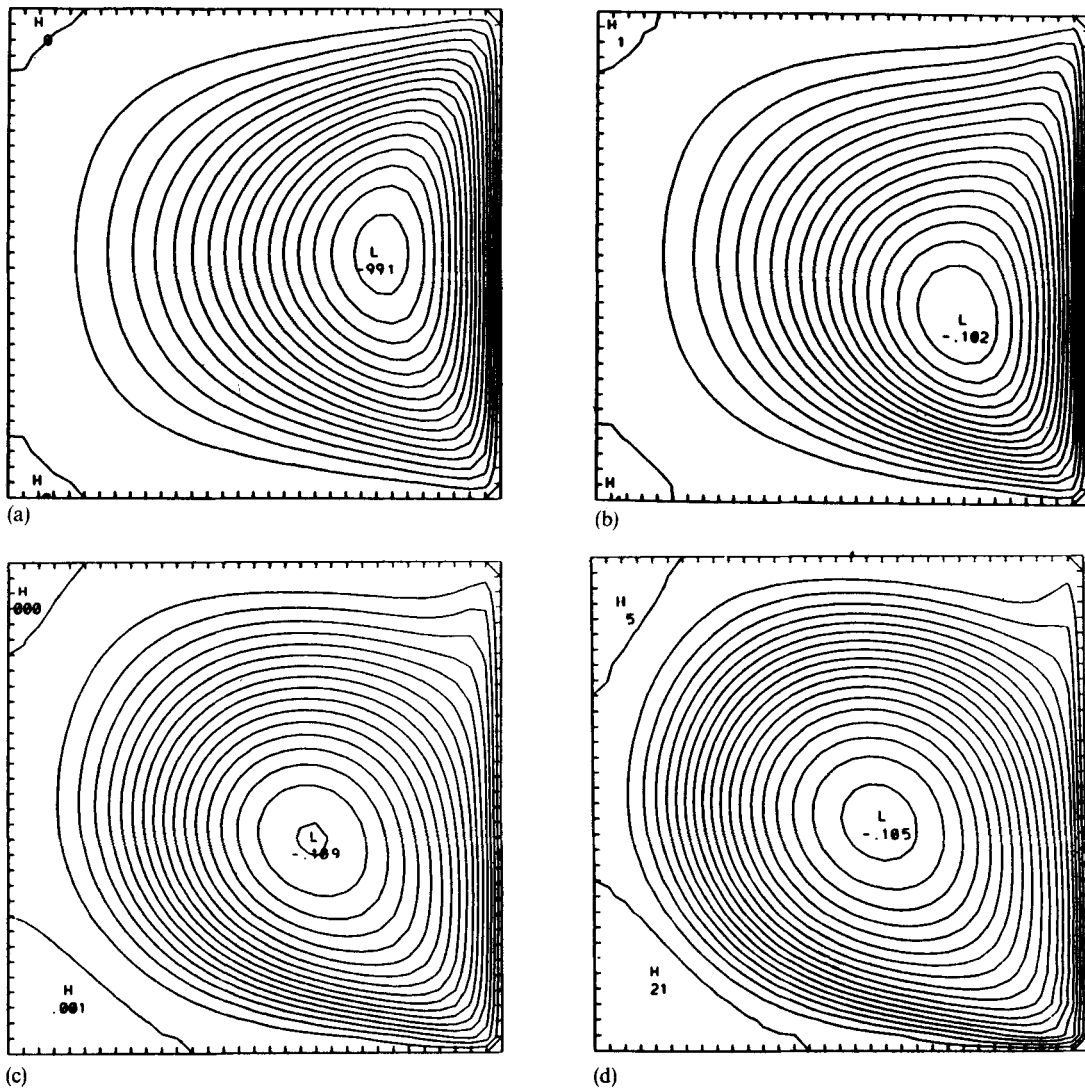


Figure 16. Streamfunction contours for the driven cavity problem, FFT results: (a) $Re = 1$; (b) $Re = 100$; (c) $Re = 400$; (d) $Re = 1000$

primary vortex centres as well as the apparent size of the secondary corner vortices compare very favourably with the results of References 17, 21 and 22. In Figures 17 and 18 vorticity contours are presented for the FD and FFT methods respectively. Note that since vorticity is a higher-order quantity, it is expected to be a more faithful indicator of numerical accuracy than velocity. At low Reynolds numbers the two sets of results essentially duplicate each other, but at higher Reynolds numbers, e.g. at $Re = 400$ and 1000 , the FFT method displays strong oscillatory behaviour, especially in the vicinity of the right lower corner, which is the critical point for this flow. This suggests that either the FFT method requires a larger number of grid points for comparable accuracy or that the no-slip boundary conditions are not adequately resolved by the polynomial

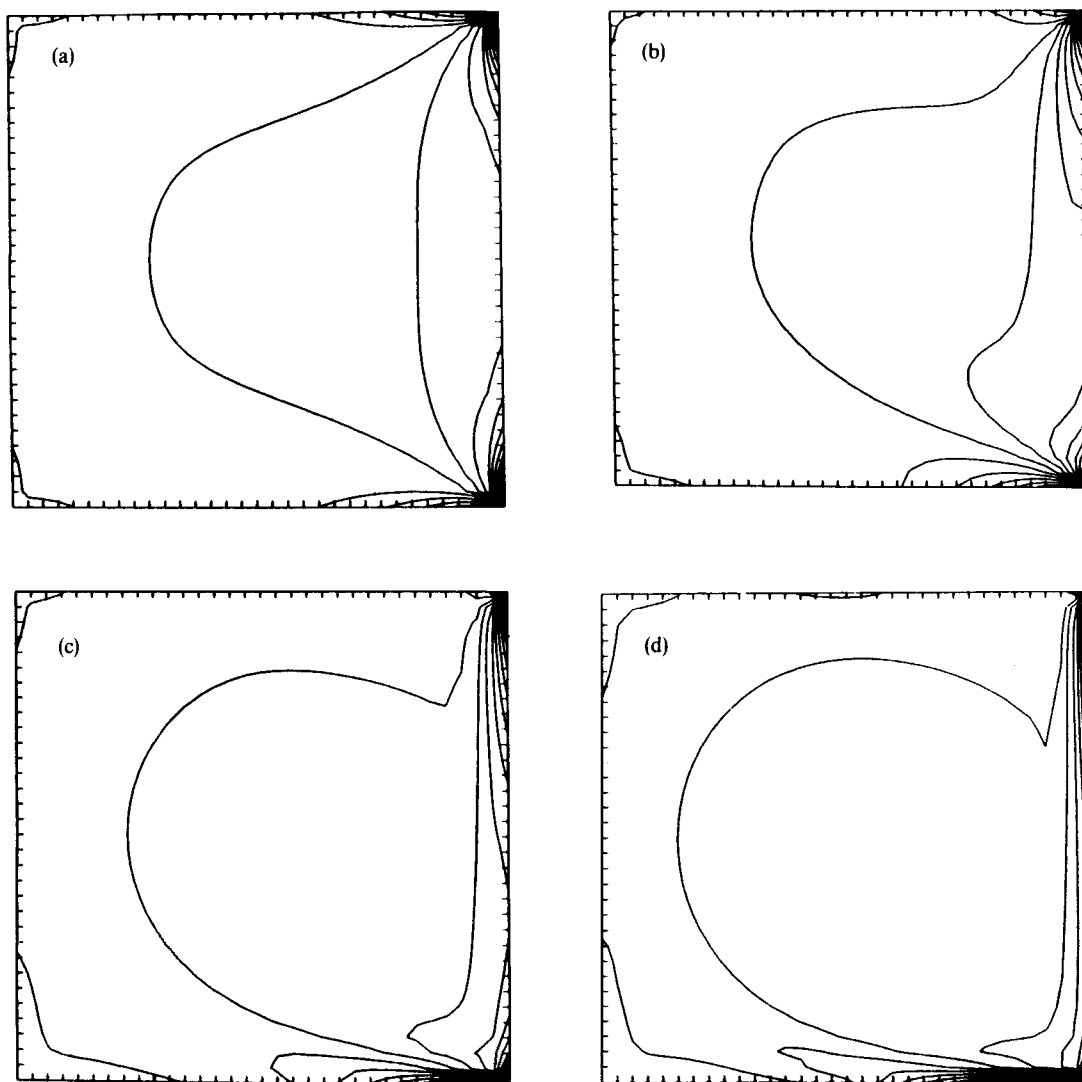


Figure 17. Vorticity contours for the driven cavity problem, FDM results: (a) $Re = 1$; (b) $Re = 100$; (c) $Re = 400$; (d) $Re = 1000$

technique (a full discussion of wiggles appearing in numerical solutions is given in Reference 23). These results are at some variance with Roache's⁷ findings, since he reports good results for the driven-cavity problem using the FFT method at low Reynolds numbers. In Figures 19 and 20 pressure contours for the FD and FFT methods are given, indicating strong similarity between the results (and no wiggles) except for several zero-level contours at $Re = 400$ and 1000 . Finally, Figures 21 and 22 present profiles of u -velocity at the cavity midplane, confirming the strong similarity between the FD and FFT methods for these low-order quantities.

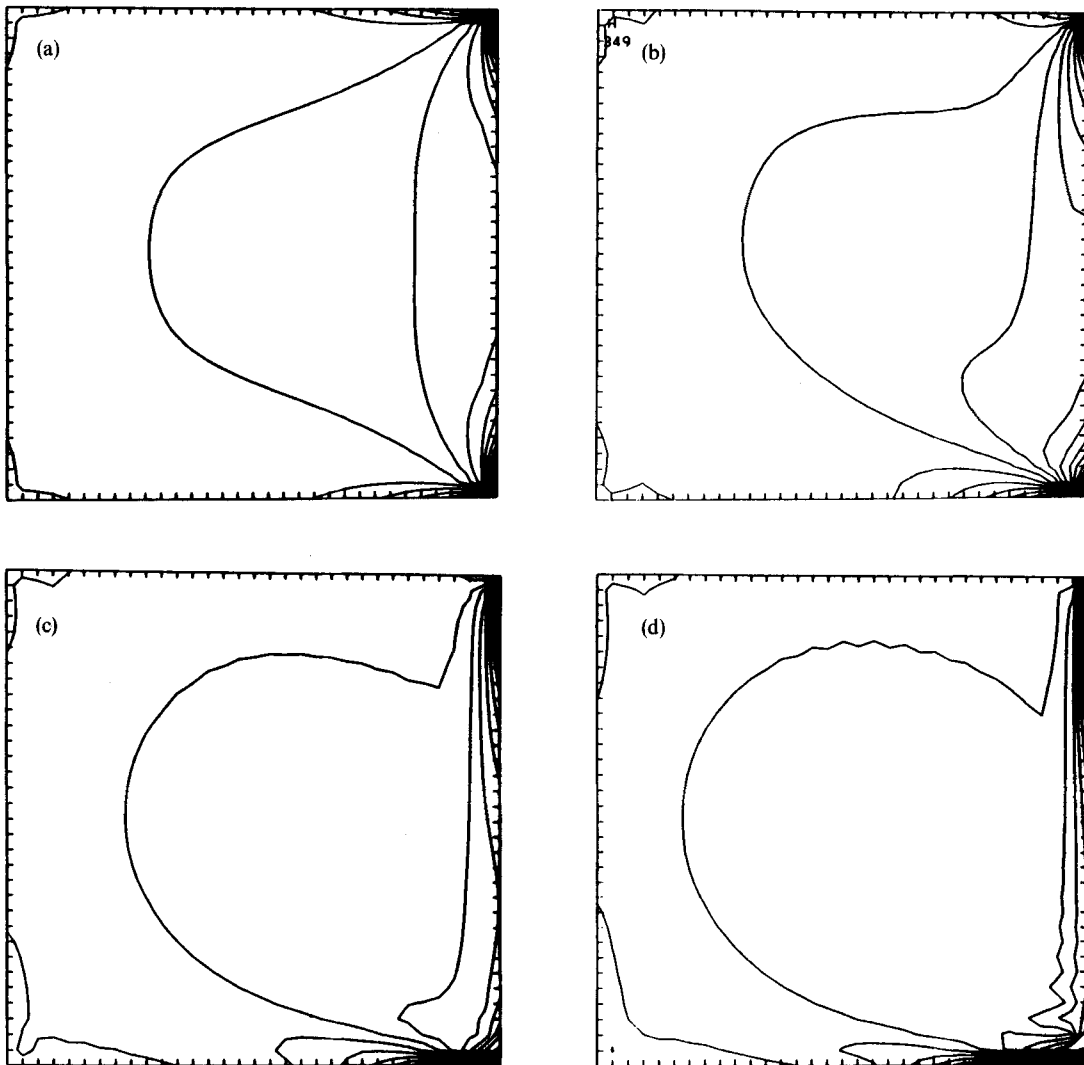


Figure 18. Vorticity contours for the driven cavity problem, FFT results: (a) $Re = 1$; (b) $Re = 100$; (c) $Re = 400$; (d) $Re = 1000$

4.2. Flow over a backward-facing step

In this section we summarize the results for the back-facing step problem, which is a frequently used test case for incompressible flow solutions. In Figure 23 a schematic diagram of the problem and the boundary conditions employed in this work are provided. At the inflow boundary a parabolic velocity profile is prescribed and the outflow boundary is located at a distance $30h$ downstream of the step. Here h is the step height and the Reynolds number is defined in terms of $2h$ and $\frac{2}{3}U$, where U is the maximum inflow velocity. Computations were performed on a 33×129 uniform mesh with zero initial conditions, and steady state solutions were obtained by

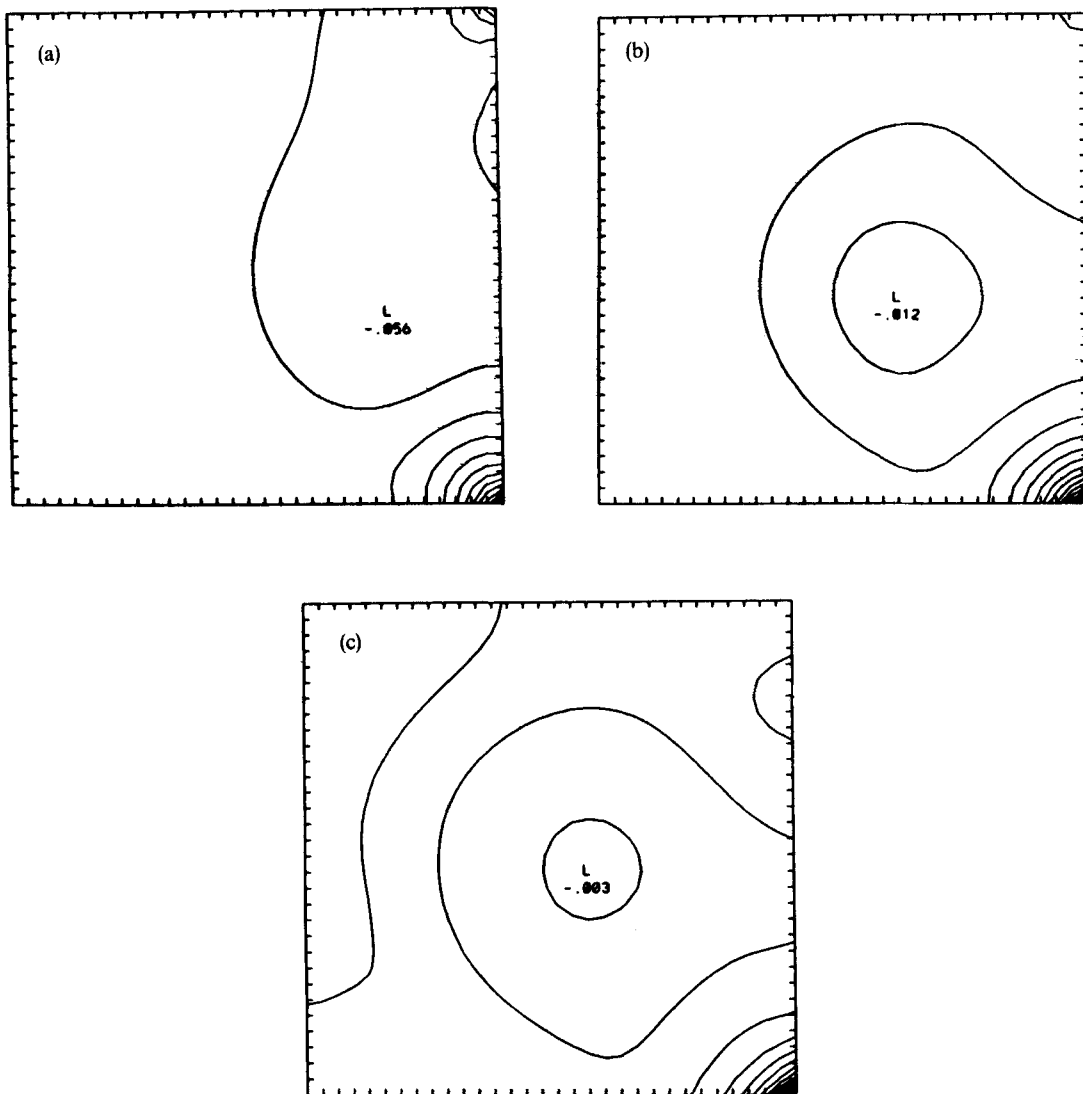


Figure 19. Pressure contours for the driven cavity problem, FDM results: (a) $Re = 100$; (b) $Re = 400$; (c) $Re = 1000$

marching in time until convergence. It should be noted that since the major goal of this computation is to provide a means of comparison between the FD and FFT methods, we have not found it necessary to conduct a mesh refinement study. However, initial numerical experiments indicated an equally poor performance for both methods on a 33×65 mesh.

The results of this investigation concerning the reattachment length x_r , are summarized in Table II, which also furnishes comparisons with experimental measurements²⁴ and other computational studies.^{17, 24} It is interesting to note that for both $Re = 267$ and $Re = 467$ the results are identical and are within a few per cent of the high-resolution computations of Reference 17 as well the measurements of Reference 24.

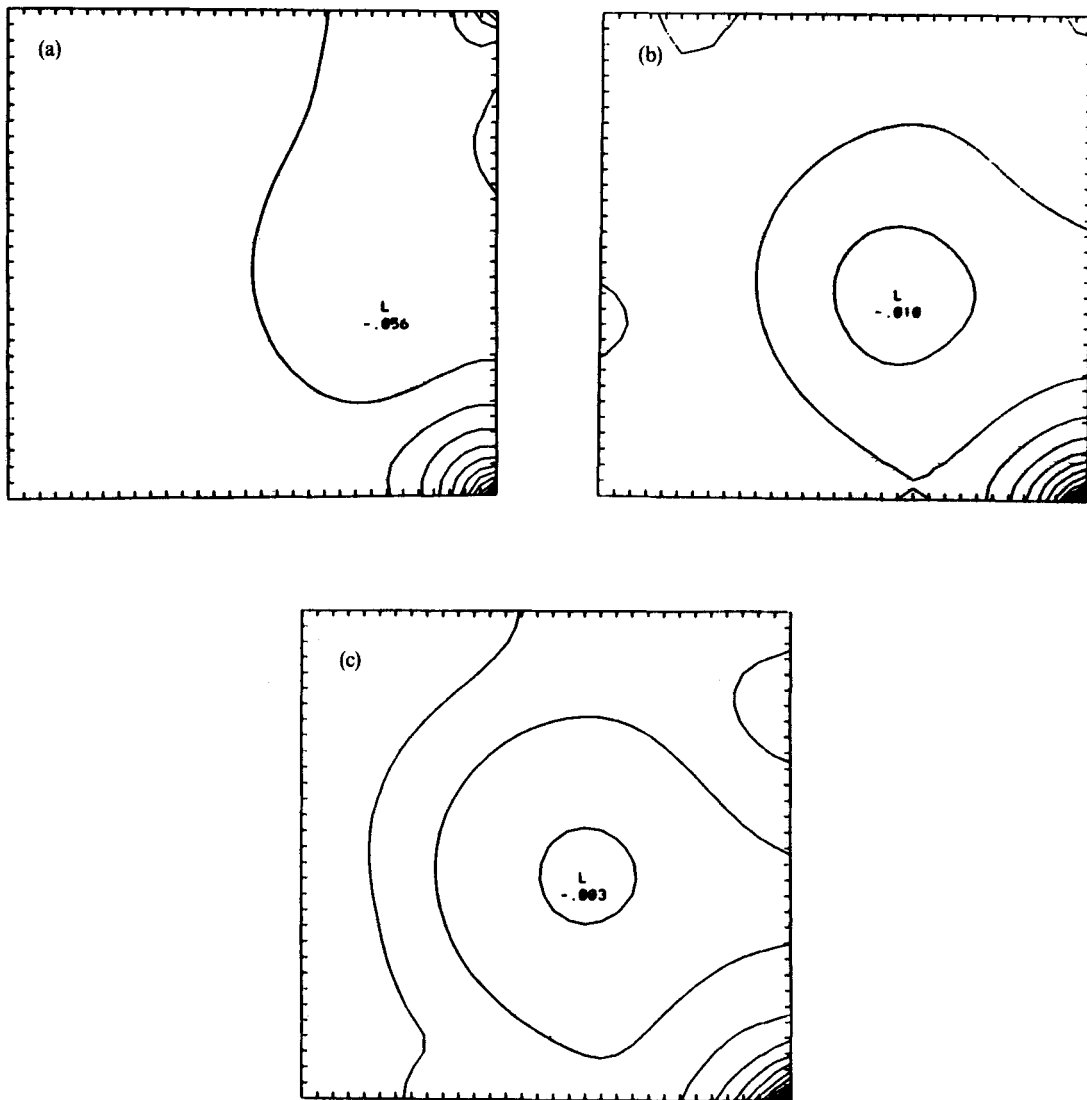


Figure 20. Pressure contours for the driven cavity problem, FFT results: (a) $Re = 100$; (b) $Re = 400$; (c) $Re = 1000$

Table II. Reattachment length—backward-facing step

Re	Present FFT	Present FD	Ref. 17 (a)	Ref. 24 (b)	Ref. 24 (c)
267	6.5	6.5	6.5	6.5	6.5
467	9.1	9.1	9.3	9.3	8.7

- (a) 130×130 uniform mesh.
- (b) Experimental measurements.
- (c) 45×45 non-uniform mesh.

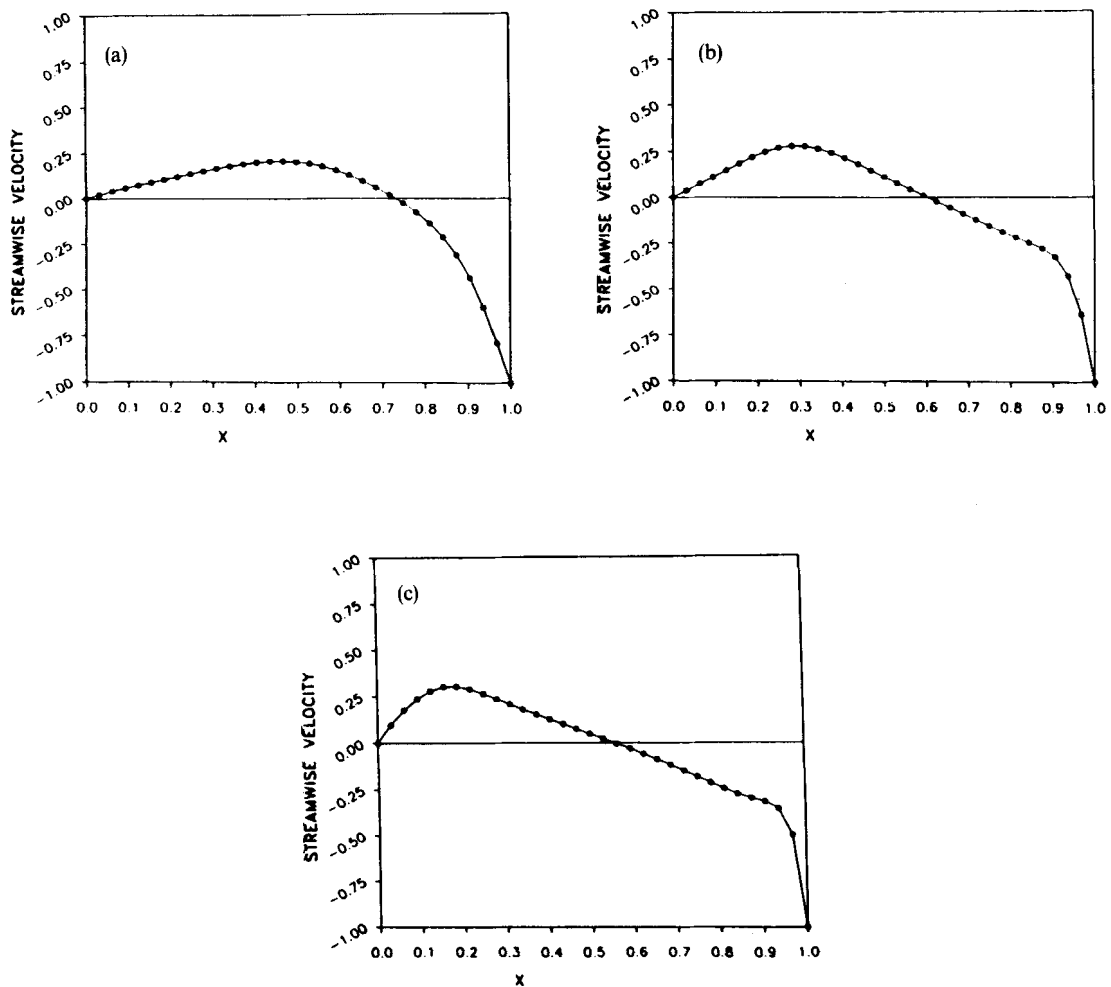


Figure 21. Streamwise velocity profiles at the midplane of the cavity, FDM solutions: (a) $Re = 100$; (b) $Re = 400$; (c) $Re = 1000$

Comparisons between the FD and FFT methods are given in Figures 24, 25 and 26, where we plot contours of streamfunction (obtained from the calculated velocity field), modified pressure and vorticity respectively. Figures 24 and 25 show that both the streamfunction and pressure results do not indicate any significant variance for both Reynolds numbers.

Consequently, it can be asserted that although the FFT method performs poorly in the presence of solid boundaries, no detectable boundary errors are observed in treating the standard inflow/outflow boundary conditions with this method. However, solutions for the back-facing step problem do not lend any evidence to the superiority of the FFT method over the FD method, with the FFT method at a cost disadvantage owing to the extra $\log N$ operation count for equal numbers of grid points.

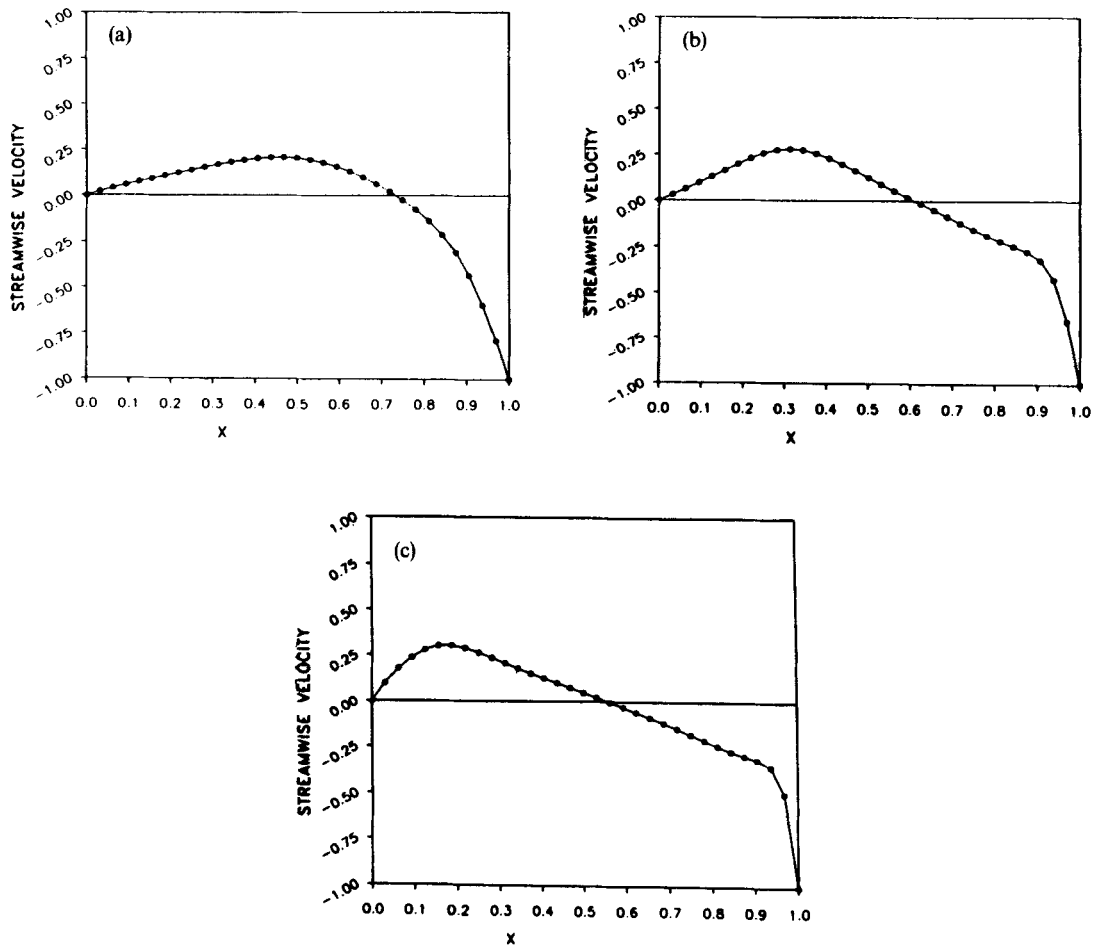


Figure 22. Streamwise velocity profiles at the midplane of the cavity, FFT solutions: (a) $Re = 100$; (b) $Re = 400$; (c) $Re = 1000$

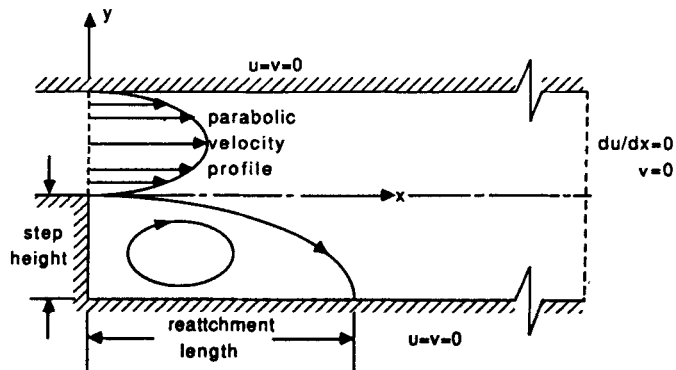
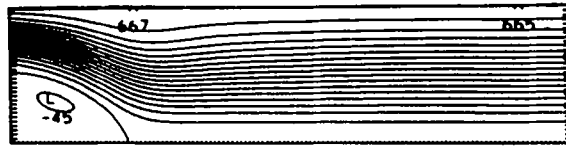
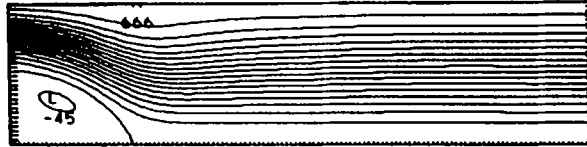


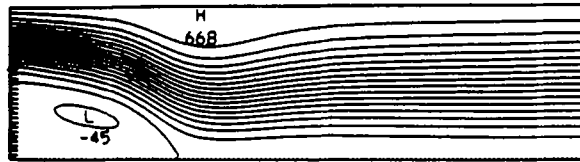
Figure 23. Schematic diagram of the back-facing step problem



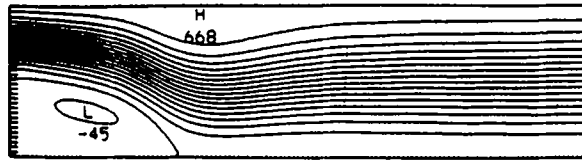
(a)



(b)

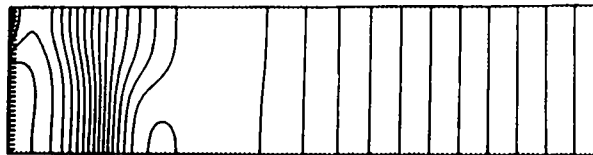


(c)

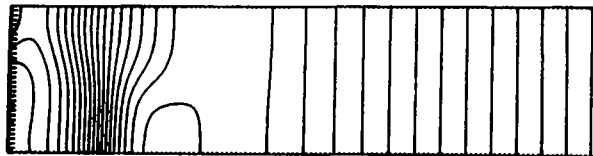


(d)

Figure 24. Streamfunction contours for the back-facing step; (a) $Re = 267$, FDM; (b) $Re = 267$, FFT; (c) $Re = 467$, FDM; (d) $Re = 467$, FFT

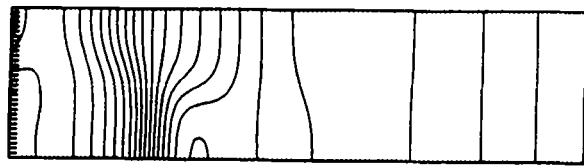


(a)

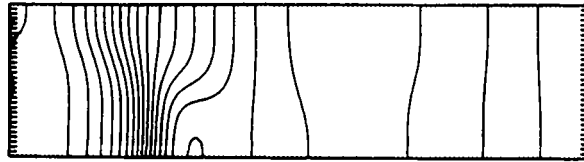


(b)

Figure 25. (a, b)

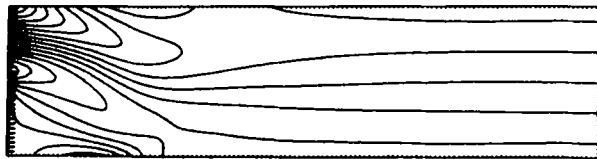


(c)

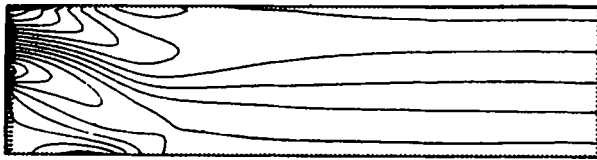


(d)

Figure 25. Pressure contours for the back-facing step; notation as in Figure 24



(a)



(b)



(c)



(d)

Figure 26. Vorticity contours for the back-facing step; notation as in Figure 24

5. CONCLUDING REMARKS

In this work we investigated the applicability of the reduction-to-periodicity method using the FFT technique to numerically integrate several partial differential equations with non-periodic boundary conditions, including the two-dimensional, time-dependent Navier–Stokes equations. We now summarize some important aspects of this study:

- (1) Based on the numerical integration of model equations, the FFT method provides marginal improvement in accuracy over a corresponding second-order FD method. At the boundaries where the FFT method is expected to have poor accuracy, however, no serious degradation of solution accuracy is revealed.
- (2) When it is implemented for the driven-cavity problem with stationary and moving solid boundaries involving no-slip boundary conditions, the FFT method displays significant errors in the vicinity of the boundaries. These errors are most apparent in vorticity contours, displaying an oscillatory behaviour at moderately high Reynolds numbers, $Re = 1000$. Consequently, we do not recommend the FFT method along directions normal to solid boundaries.
- (3) In the back-step problem the FFT method resolves the standard inflow/outflow boundary conditions to the accuracy of the second-order FD method. For both methods, even at moderately high Reynolds numbers, the calculated reattachment length is within a few per cent of measured values. Consequently, this method is applicable for problems with inflow/outflow boundary conditions of the type used in the backward-facing step problem, but the cost of using the FFT method over a second-order finite difference method for the problems investigated could not be justified. However, owing to minimum phase errors of the spectral discretization, the FFT method may prove to be feasible to implement in wave propagation problems with non-linear wave interactions, as suggested by the work of Patera.⁹ Even then, the application of this method to full-scale calculations can be justified only after it can furnish favourable comparisons with true spectral methods applicable to non-periodic inflow/outflow boundary conditions (see e.g. Macaraeg and Streett²⁵ and Patera²⁶). This issue is currently under investigation.

ACKNOWLEDGEMENTS

This work was performed under Grant NAG-1-798 from NASA/Langley Research Center and with partial support from the AFOSR under Grant 81-0037. The authors are grateful to P. J. Bobbitt and W. D. Harvey for their continued interest and to the two referees who reviewed this paper for their helpful comments.

REFERENCES

1. S. A. Orszag, 'Numerical methods for the simulation of turbulence', *Phys. Fluids Suppl.*, **II**, 250–257 (1969).
2. S. A. Orszag, 'Numerical simulation of incompressible flows within simple boundaries: accuracy', *J. Fluid Mech.*, **49**, 75 (1971).
3. S. A. Orszag, 'Numerical simulation of incompressible flows within simple boundaries Galerkin representation', *Stud. Appl. Math.*, **L**, 293–327 (1971).
4. S. A. Orszag and M. Israeli, 'Numerical simulation of viscous incompressible flows', *Ann. Rev. Fluid Mech.*, **6**, 281–318 (1974).
5. C. Lanczos, *Applied Analysis*, Prentice-Hall, Englewood Cliffs, NJ, 1956.
6. D. Gottlieb and S. A. Orszag, 'Numerical analysis of spectral methods: theory and applications', *NSF-CBMS Monograph No. 26*, SIAM, Philadelphia, PA, 1977.
7. P. J. Roache, 'A pseudo-spectral FFT technique for non-periodic problems', *J. Comput. Phys.*, **27**, 204–220 (1978).
8. H. Wengle and J. H. Scinfeld, 'Pseudospectral solution of atmospheric diffusion problem', *J. Comput. Phys.*, **26**, 87–106 (1978).

9. A. T. Patera, 'Spectral methods for spatially evolving hydrodynamics flows', in *Spectral Methods for Partial Differential Equations*, SIAM, Philadelphia, PA, 1984, pp. 239–256.
10. D. K. Lilly, 'On the computational stability of numerical solutions of time-dependent non-linear geophysics fluid dynamics problems', *Mon. Weather Rev.* **93**, 11–26 (1965).
11. P. J. Roache, *Computational Fluid Dynamics*, Hermosa, Albuquerque, NM, 1972, p. 74.
12. J. H. Williamson, 'The low-storage Runge–Kutta schemes', *J. Comput. Phys.*, **35**, 48–56 (1980).
13. T. A. Zang and M. Y. Hussaini, 'A three-dimensional spectral algorithm for simulations of transition and turbulence', *ICASE Report No. 85–19*, 1985.
14. E. R. Beutson and G. W. Platzman, 'A table of solutions of the one-dimensional Burgers equation', *Q. Appl. Math.*, **30**, 195–212 (1972).
15. P. S. Lowery and W. C. Reynolds, 'Numerical simulation of a spatially developing, forced, plane mixing layer', *Report No. TF-26*, Stanford University, September 1986.
16. M. Fortin, R. Peyret and R. Temam, 'Resolution numerique des equations de Navier–Stokes pour un fluide incompressible', *J. Mecanique*, **70**, 439–462 (1971).
17. J. Kim and P. Moin, 'Application of a fractional-step method to incompressible Navier–Stokes equations', *J. Comput. Phys.*, **59**, 308–323 (1985).
18. F. H. Harlow and J. E. Welch, 'Numerical calculation of time-dependent viscous incompressible flow of fluid with free surface', *Phys. Fluids*, **8**, 2182–2189 (1965).
19. S. Biringen, G. Danabasoglu and L. J. Peltier, 'Influence of G-jitter on thermal convection at 1G and micro-G environment', *Bull. APS*, **32**, 2025 (1987).
20. H. A. Dwyer, K. Matsuno, S. Ibrani and M. Hafez, 'Some uses of direct solvers in computational fluid dynamics', *AIAA Paper 87–0594*, 1987.
21. U. Ghia, K. N. Ghia and C. T. Shin, 'High Re solutions for incompressible flow using the Navier–Stokes equations and a multigrid method', *J. Comput. Phys.*, **48**, 387–411 (1982).
22. R. Schreiber and H. B. Keller, 'Driven cavity flows by efficient numerical techniques', *J. Comput. Phys.*, **49**, 310–333 (1983).
23. P. M. Gresho and R. L. Lee, 'Don't suppress the wiggles—they're telling you something', *Comput. Fluids*, **9**, 223–253 (1981).
24. B. F. Armaly, F. Durst, J. C. Pereira and B. Schönung, 'Experimental and theoretical investigation of backward-facing step flow', *J. Fluid Mech.*, **127**, 473–496 (1983).
25. M. G. Macaraeg and C. L. Streett, 'Improvements in spectral collocation discretization through a multiple domain technique', *Appl. Numer. Math.*, **2**, 95–108 (1968).
26. A. T. Patera, 'A spectral element method for fluid dynamics: laminar flow in a channel expansion', *J. Comput. Phys.*, **54**, 468–488 (1984).